Title: Experimental and numerical studies on dynamic stress and curvature in steel tube umbilicals

Authors: Tianjiao Dai[a], Svein Sævik[a] and Naiquan Ye[b]

[a] Department of Marine Technology, Norwegian University of Science and Technology, NO-7491 Trondheim, Norway

[b] OIL and GAS, SINTEF OCEAN, Trondheim, NO-7052, Norway

Abstract

The present paper addresses the stresses in dynamic steel tube umbilicals at the platform hang-off exposed to large motions corresponding to an extreme storm condition. Experimental tests were carried out by mounting fibre-optic Braggs inside steel tubes of a 9m long umbilical specimen. Then the specimen was exposed to constant tension and dynamic curvature by means of a bellmouth and the stresses were measured. Realizing that the geometry of the umbilical cross section was too complex to apply full 3D modeling, a beam and penalty contact modeling procedure was applied to describe the extreme stress behavior. Then a simplified method was proposed to determine the contact stiffness which was further validated by full scale umbilical axial stiffness testing. As hoop contact interfaces between steel tubes and separation fillers were observed in the test specimen, a tailor-made contact element was formulated to facilitate hoop contact. Different modeling alternatives were used to investigate the hoop contact effect on the extreme axial stress and Coulomb friction stress range, which were further validated against measured dynamic axial stress. Good correlation was found by the combination of describing all contact interfaces and constraints due to the grooves in the inner sheath.

key words: umbilical, friction stress, axial stress, fatigue

1. Introduction

Subsea umbilicals have multiple functionalities in the subsea system application. They are mainly designed for subsea control and monitoring, chemical injection, fluid transportation, gas release and power transmission, etc. An umbilical consists of multiple groups of functional elements, such as electrical cables, optical fibre cables, hoses, steel tubes or fillers in the core, tensile armors for mechanical strength and ballast as well as the sheaths for protection and compactness. This determines several functional components in the cross section and involves different materials including metallic, extruded polymeric and fibres, etc. Due to multiple contacts between arbitrary components of different materials, stress analysis is very challenging with respect to accuracy, stability and computation time. The finite element method with full 3D modeling by solid finite element is the only alternative that can capture all nonlinearities in terms of geometry, material, end conditions and cross section arrangement, etc. However, this will result in a large number of degrees of freedom and long computation time. Further due to the contact between steel and plastic materials, for example, between steel and fillers, the large difference in material stiffness will introduce numerical instability issues. Noting that the longitudinal stress is the primary stress component of the helical elements, the strategy adopted in the present work has therefore been based on beam and beam penalty contact elements [1].

Several authors have investigated the cross section's internal stiffness capacity effect on the axial stress of helical components. Yue et al.[2] carried out tension tests for a flexible pipe and investigated the radial stiffness of the pressure armor effect on the tensile stiffness of the tensile armor layer. The decreased tensile stiffness was found with decreasing radial stiffness. Almeida et al.[3] did stress analyses of individual components in two different layout cross sections of umbilicals and a reduction 53% of hose stress was demonstrated when the free gap was considered between hoses and inner sheath. The internal stiffness capacity of an umbilical is normally less than that of a non-bonded flexible pipe due to the relatively soft core. Lu [4, 5] and Yang et al.[6] carried out finite element analyses of umbilicals for verifying the layout methodology considering nonlinear geometry, components compactness, materials and symmetry distribution by ensuring the contact pressure and radial displacement as small as possible. Custódio and Vaz [7] performed local axisymmetric analysis of non-bonded composite cables and pipes for considering the material and geometrical nonlinearities due to gap formation and lateral contact between wires. It was found that the radial contraction reduced the available gap between wires and the cable became stiffer when the wires touched together. Since the further radial contraction was constrained and the gap between two layers of wires may be increased, the contact pressure was reduced. It was found that the internal flexibility is directly determined by the components' motion, geometry, material and cross section arrangement, etc. Therefore, the beam contact models should be capable to capture these effects by formulating this behavior into the contact stiffness and beam kinematics.

There are few works reported concerning full scale measurements of the helical component's stress behavior. Probyn et al.[8, 9] performed tensile, bending and crush full scale tests and validated the 3D FEA analysis against the test results. Good correlations with respect to umbilical bending stiffness were obtained within elastic strain of steel tubes. However, the bending tests mainly focused on global bending moment and curvature history in a three points bending rig instead of measuring stress history of individual components. Knapp and Terry [10] emphasized that the radial deformation had an important effect on the axial strain as well as axial stiffness and good correlations were obtained in terms of axial strain and torque of the whole cable cross section under different tension levels between tests and the numerical model. Dobson et al.[11] reported a full scale test measuring individual steel tube by locating strain gauges at the steel tube's outer wall and the same strain gauge concept was applied in [12] where encouraging correlation between numerical model and test results of axial strain range for moderate prescribed curvatures was obtained. However, these tests were limited to measure each steel tube's local curvature. The local curvature was measured by locating two strain gauges in the inner wall of steel tubes and reported by Ekeberg and Dhaigude [13, 14]. In some power cable tests [15, 16], the tensile armors were instrumented with strain gauges through small windows on the outer sheath. A full scale test of a dynamic steel tube umbilical was carried out as part of the Umbilical JIP Phase II [17] in Marintek (SINTEF OCEAN, today) to measure the steel tube's axial strain and local curvature by post mounting four optic fibres in the steel tube's inner wall with 90° spacing in the circumferential direction. This test is used as a reference in the present work.

The objectives of the present work are summarized as follows:

1. Present the full scale tests [17, 18] carried out in SINTEF OCEAN and calculate the instrumented steel tubes' axial strain and local curvatures.
2. Perform the global numerical analyses for quantifying some test setup parameters including the gap between the bellmouth entrance and the specimen's outer sheath as well as the contact stiffness of the bellmouth surface, which are further applied in the local analysis.
3. Propose an analytical contact stiffness method for calculating contact stiffness of internal contact interfaces.
4. Propose a hoop contact element and implement it into the computer code BFLEX [1, 19].
5. Perform numerical analyses by using different modeling alternatives for investigating hoop contacts effect on the dynamic stress behavior and fatigue life prediction.

2. Experimental study

2.1. Test set-up

The test set-up is shown in Figure 1. It consisted of the umbilical specimen, adapter (extension piece for fitting the specimen to the load cell), rig components (rocking head, tower, bellmouth, tensioner actuator, logging system). The tower rig, specimen cross section and bellmouth are shown in Figure 2. The full scale umbilical specimen was delivered with two end fittings. The tensioner was used to apply constant tension at the specimen right end. Four tension levels were applied to the specimen, 5, 100, 200 and 300KN. Two bellmouths were fixed to the tower rig and rotated to apply bending loads to the umbilical. In the present work, only the second bellmouth with constant curvature 0.1 [1/m] was reported because the relatively large curvature may introduce significant nonlinear 3D effects on the helices when the specimen has full contact.

2.2. Specimen

A steel tube umbilical cross section is usually composed of functional components made of steel materials which are helically wound around a central core. The core may be a plastic or steel tube. Figure 3 presents the idealized geometry of the umbilical specimen at two measured sensor stations in this test. The cross section consisted of a main center tube, three large helical tubes, nine small helical tubes, twenty-one fillers, three sheath layers and two tensile armor layers, which were symmetrically arranged. The sheath over the center tube and fillers were used for separating direct contact between the large helical tube, center tube and small helical tubes. In addition, fillers were applied to fill out the interstitial voids between components for maintaining a compact and circular cross section. The helical tubes were wound together with the same lay angle, 7°. This bundle was over-sheathed by extruding an intermediate sheath. Two cross wound layers of tensile armors were arranged for avoiding substantial axial stress in the steel tubes. The tensile armors were covered by an outer sheath layer providing mechanical protection. The corresponding components' dimensions and radial locations are presented in Table 1.

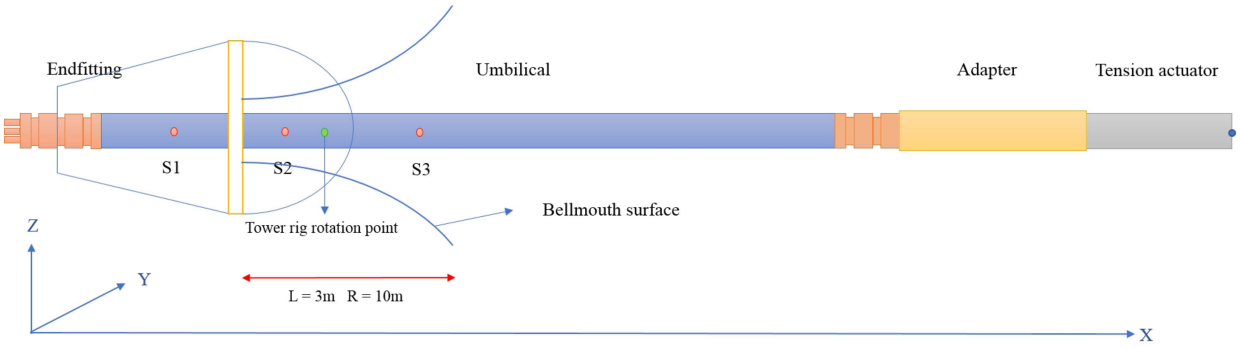

Figure 1: The test setup sketch

Tower rig | Specimen cross section | Specimen and bellmouth

Figure 2: The tower rig, specimen cross section and bellmouth in the full scale testing

Table 1: Components' dimension in the specimen cross section

Tube Name	Radial location [mm]	Outer diameter [mm]	Thickness [mm]	Pitch length [mm]
Center tube	0	44.1	3	1875
PE Inner sheath	0	50.1	3	–
Small tube	44.5	17.9	2.6	1875
Large tube	39.25	28.4	1.5	1875
Round polymeric filler	30.3	–	–	1875
Interstitial polymeric filler	44.3	–	–	1875
HDPE Mid sheath	0	55.45	4	–
Outer armor layer	63.62	–	3.5	1380
Inner armor layer	59.62	–	3.5	-775
HDPE Outer sheath	0	67.6	4	–

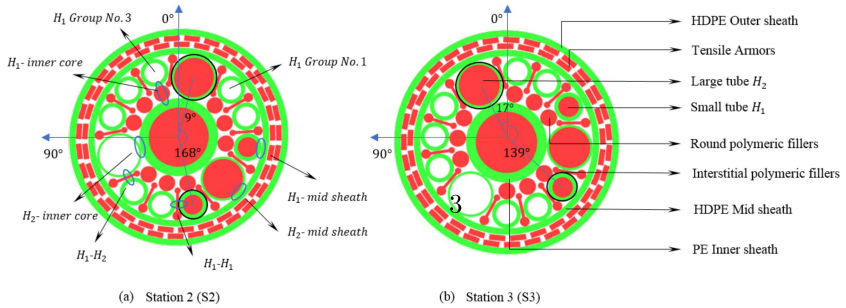

(a) Station 2 (S2) (b) Station 3 (S3)

2.3. Optic fibre sensor stations

Three types of tubes were instrumented: the center tube, the large helical tube and the small helical tube. Three fibre bragg-grated (FBG) sensor stations were post mounted in the selected tubes by inserting steel bars where sensors were mounted. The sensor stations were then fixed to the inner wall by epoxy glue. The sensor station locations were selected according to the bellmouth length. The first station (abbreviated as S1) was positioned 0.95m away from the left end of umbilical and outside the bellmouth surface where small curvature was expected. The second station S2 was 0.675m away from the bellmouth entrance and the third station S3 was 0.352m away from the bellmouth end, see Figure 1.

Figure 4 presents the plastic spacing device which was used to mount four sensors in the tube's circumferential direction with 90° resolution and positioned parallel to its longitudinal axis. Then the local curvature of each instrumented tube can be obtained based on these four individual signals. Each optic fibre sensor should be located as far as possible from the tube center in order to guarantee the bending signals quality. The spacing device diameter was slightly less than the inner diameter of the corresponding instrumented tube to ease the post-installation.

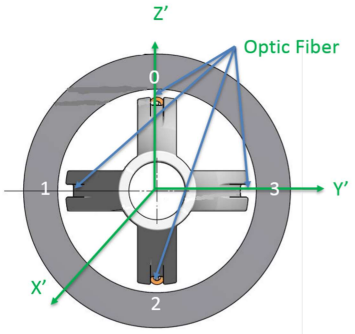

Figure 4: The spacing device for mounting the optic fibres

2.4. Post-processing of test data

The FBG is fabricated for reflecting a particular wavelength of light and transmitting all other ones. It is only constructed along a small segment of optic fibre at the sensor station. The strain of each optic fibre can be transformed from the change in wavelength due to the imposed strain. The axial strain at the center of the spacing device was calculated as the average of four strains from the optic fibres of each tube at each station. Additionally, the curvature around Y axis (κ'_y) and curvature around Z axis (κ'_z) of the spacing device can be obtained from the corresponding two opposite strain sensors seen in Eq. 2 and Eq. 3, respectively. Since the spacing device was post-mounted at each sensor station and fixed by epoxy, there had to be sufficient tolerance margins between the spacing devices and tubes' inner wall, resulting in eccentricities between the spacing device center and tube center. These eccentricities can be measured on the cross section by the specimen dissection. Therefore, the axial strain of tube in the center should be corrected based on the eccentricities and curvatures, given by Eq. 4.

Numerical studies were carried out in BFLEX, see Section 5. Figure 5 presents the global coordinate system of the test setup, the local coordinate system of tubes, and the spacing device coordinate system which are illustrated by the yellow, red and green colors, respectively. In order to be consistent with the local coordinate system defined in BFLEX, the curvatures measured in the spacing device coordinate system had to be transformed to the local coordinate system of the tube based on the measured angles between these two coordinate systems in the cross section after dissection. The curvatures in local system were obtained by the curvatures in the spacing device coordinate system and the transformation tensor as shown in Eq. 5.

The axial strain and curvature of tube in spacing device coordinate system are calculated as below:

$$\epsilon'_a = \frac{\epsilon'_0 + \epsilon'_1 + \epsilon'_2 + \epsilon'_3}{4} \tag{1}$$

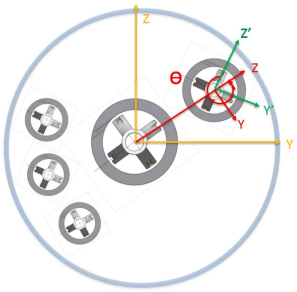

Figure 5: Global coordinate system of umbilical, local coordinate system of tube and coordinate system of spacing device

$$\kappa_y' = \frac{\epsilon_0' - \epsilon_2'}{z_0' - z_2'} \tag{2}$$

$$\kappa_z' = \frac{\epsilon_1' - \epsilon_3'}{y_3' - y_1'} \tag{3}$$

The axial strain and curvature of tube in the local coordinate system is shown in the following:

$$\epsilon_a = \epsilon_a' - (\kappa_y' z_e - \kappa_z' y_e) \tag{4}$$

$$\begin{bmatrix} \cos\theta & \sin\theta \\ -\sin\theta & \cos\theta \end{bmatrix} \begin{bmatrix} \kappa_z' \\ \kappa_y' \end{bmatrix} = \begin{bmatrix} \kappa_z \\ \kappa_y \end{bmatrix} \tag{5}$$

Where y_e and z_e are eccentricities between center of spacing device coordinate system and local coordinate system of the tube, θ is the angle rotated from spacing device coordinate system to local coordinate system.

3. Hoop contact model

As the hoop contacts were observed between the steel tubes and separation fillers in Figure 3, the hoop contact element was tailor-made and implemented into BFLEX and the HCONT454 element as shown in Figure 6. The method outlined in [20, 21] was used which is based on the concept of an Incremental Potential for including the constraint conditions between two bodies in contact. Referring to a Cartesian coordinate system, $x_i, i = 1, 2, 3$, the energy functional $\Delta\pi$ includes both terms related to the bodies A and B alone and terms associated with the contact conditions:

$$\Delta\pi = \sum_{l=A}^{B} \Delta\overline{\pi}^l - \int_{S_C} (\lambda_n + \Delta\lambda_n) \cdot g ds - \frac{1}{2\alpha_C} \int_{S_C} \Delta\lambda_n^2 ds - \int_{S_C} \lambda_t \cdot \Delta\gamma ds - \frac{1}{2} \int_{S_C} \Delta\lambda_t \Delta\gamma ds \tag{6}$$

Where $\Delta\pi^l$ is the incremental potential of bodies A and B alone, λ_n is the contact pressure and λ_t is the shear stress acting on the contact surface S_c. λ_t has to be based on the constitutive relation established related to friction. α_C is a scaling parameter related to the contact stiffness, assuming that the surface behaves elastic. g is the gap and γ is the tangential relative displacement.

For the two bodies to be in equilibrium at any instant within a time interval $[t, t + \Delta t]$, it is necessary to require:

$$\delta\Delta\pi = 0 \tag{7}$$

By carrying out the above variational procedure, the following constraint condition is recovered in addition to the traditional Euler equations and boundary conditions:

$$(\Delta \boldsymbol{u}_B - \Delta \boldsymbol{u}_A) \cdot \boldsymbol{n} + g_0 = \frac{\Delta\lambda_n}{\alpha_C} \tag{8}$$

Eq.8 represents a weak condition and the exact contact condition can only be recovered if $\alpha_C \to \infty$. Then for a given α_C, Eq.8 can be used to define the unknown contact pressure λ_n. The initial gap g_0 in the local helix X^2 direction at the time $t = 0$ can be approximated by:

$$g_0 = b(\frac{1}{F_f} - 1) \tag{9}$$

where b is the helix width and F_f is the layer fill factor defined by $F_f = \frac{nb}{\cos\alpha 2\pi R}$ where n is the number of helices in the same layer, α is the lay angle and R is the layer radius. Then the gap increment between t and $t + \Delta t$ is influenced by the incremental transverse displacement, radial and bending motions as:

$$g = \Delta u_2^B - \Delta u_2^A + \frac{b}{F_f}(\Delta\varepsilon_\psi + \Delta\varepsilon_{Z^1}) + g_0 \tag{10}$$

$\Delta\varepsilon_\psi$ is the hoop strain taken to be:

$$\Delta\varepsilon_\psi = \frac{1}{2R}(\Delta u_3^B + \Delta u_3^A) \tag{11}$$

$\Delta\varepsilon_{Z^1}$ is obtained from the supporting pipe global curvature as:

$$\Delta\varepsilon_{Z^1} = -Rsin\psi\Delta v_{,11} + Rcos\psi\Delta w_{,11} \tag{12}$$

where v and w are the transverse motion displacements of the umbilical center, see Figure 6. $_{,11}$ denotes differentiation with respect to the longitudinal pipe centerline coordinate Z^1, see Figure 7.

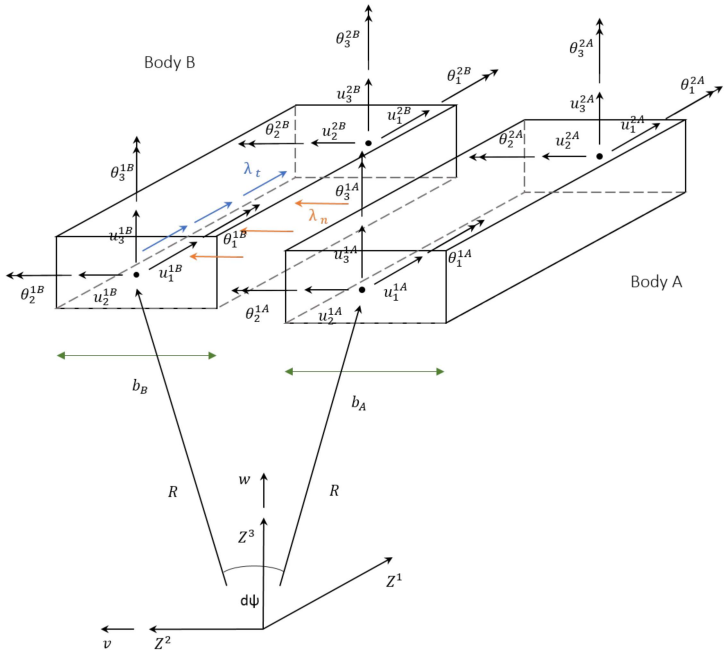

Figure 6: Hoop contact element HCONT454

4. Global analysis

Global analyses were carried out to evaluate the uncertain parameters in the test setup and verify the bellmouth geometry model in BFLEX. Figure 8 presents the global model consisting of umbilical, end fitting, load cell, adapter, tension actuator and bellmouth represented by the green surface. The full contacts between bellmouth surface and specimen in the tests are shown in Figure 8b and 8c. All parts were modeled by 354 elastic beam elements. The mechanical properties of the umbilical was obtained from UFLEX [22] by modeling each component in the cross section.

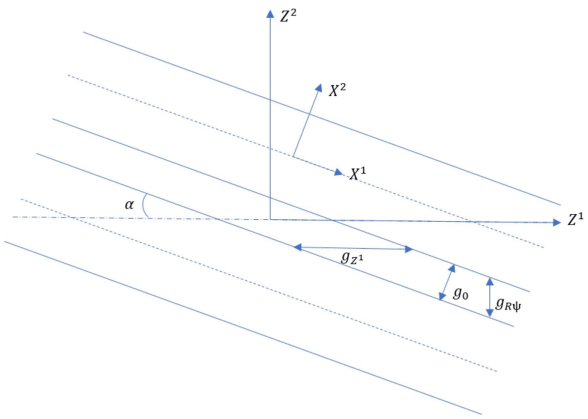

Figure 7: The gap definition in the hoop direction for the hoop contact element HCONT454

The end fitting, load cell and adapter elements were modeled by associating the elements with large axial, bending and torsion stiffnesses. The weight of these components were set to zero due to the weight compensating procedures applied in the test. The tensioner was free to rotate and the bending loads induced longitudinal displacement of the specimen was compensated by the tensioner elongation. Therefore, constant tension was recorded in all load cases in the tests. This physical property was achieved by modeling the beam element with small axial stiffness and applying the initial strain concept to obtain constant tension. The tension 200KN and self-weight of umbilical were applied before moving the bellmouth according to the full scale test procedure. A rigid link was established between the first umbilical element and the pivot point to simulate the rigid tower head by the element eccentricity.

The bellmouth geometry was generated based on a given curvature and length. The contact between the bellmouth surface and the umbilical was handled by the penalty based beam to surface contact element HCONT152 with a sufficient contact stiffness to obtain correct curvature without convergence problems. A sensitivity study was then carried out to determine this contact stiffness. It was found that as long as the stiffness is larger than 1E8 $[N/m^2]$, good correlation with the bellmouth surface curvature was obtained. The value of 1E8 was therefore used in following simulations.

In addition, the gap between the bellmouth entrance and the outer sheath should also be determined in the global analysis, since it was not measured in the test. As the gap was in an order of 5mm, a sensitivity study with respect to the gap was performed where the gap was set to be 1, 3, 5 and 8mm. Figure 9 presents comparison results between the center tube's curvature in the tests and umbilical global curvature obtained from simulations at S2 and S3 under tension 200KN. It is noted that the curvatures at two stations were not sensitive to the gap as long as the gap is smaller than 8mm. A gap equal to 3mm was then used in the local stress analyses. It was also found that the specimen curvature increased with rocking angle until about 7° and then maintained constant. This implies that the specimen starts to fully contact with the bellmouth surface at 7° and stays on the surface afterwards. Since the tension 200KN is sufficient to ensure full contact between the bellmouth and specimen, the value was further used in the 3D local stress analyses.

5. 3D Local stress analysis

5.1. Specimen cross section model

As there existed significant 3D effects in the tests including end effects, nonlinear and time-varying curvature distribution along the pipe, modeling of each helix over the full length was needed. In addition, the cross section is complex including multiple contact interfaces between different materials. The sandwich beam theory together with the penalty contact method was therefore adopted in the present work. Then 3D FE models were established to simulate the full scale testing in BFLEX. Figure 10 shows the individual modeling of each helix in the umbilical specimen cross section. The cross section parameters are presented in Table 1. Each component was modeled as an individual part except the fillers. The tensile wires and steel tubes were modeled by the curved beam element HSHEAR353 [1, 19]. The outer and intermediate sheathes were modeled by the HSHEAR363 element. This is a thin

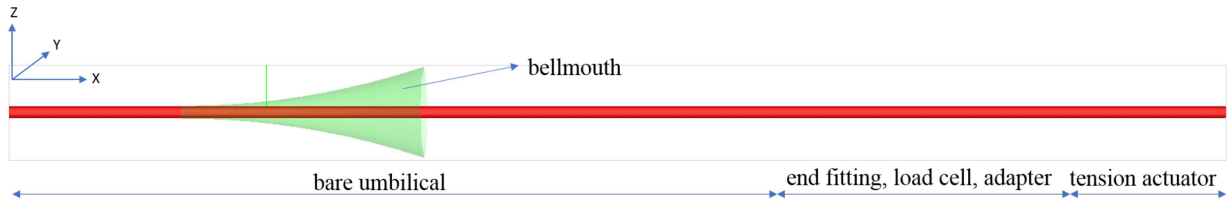

(a) Global model of full scale testing in BFLEX

(b) The umbilical has full contact with upper surface of bellmouth

(c) The umbilical has full contact with lower surface of bellmouth

Figure 8: Global model of full scale testing in BFLEX and the full contact condition between umbilical and bellmouth surface

shell/beam element including 3 nodes where 2 nodes (12 DOFs) are associated to the standard beam element which enables modeling torsion, bending and axial behavior of the sheath layers and 1 node (1 DOF) is used to describe the shell radial motion by means of the thin shell theory and the two dimensional version of Hooke's law. Based on mesh sensitivity study, the umbilical section was divided into 90 segments.

Since all functional components including tensile armors and steel tubes were modeled by beam elements, the interaction surfaces were modeled by penalty line contact elements to describe the inherent flexibility between components. The contact elements operate in the local surface system and include eccentricities, contact stiffness and friction effects, which calculate the contact line force and the friction by alternative friction models. The detailed features of curved beam and line contact elements have been described previously and are not repeated here, see [23, 24]. However, a brief summary of the modeling is given. The purpose of HCONT453 and HCONT454 are to describe radial and hoop contacts between two helical elements modeled by HSHEAR353. Since a beam element approach is adopted, local deformations due to filler contact needs to be built-into the penalty parameter of the contact element. HCONT463 element is used to establish the contact between the concentric layers modeled by HSHEAR363 and the helical element modeled by HSHEAR353. The HCONT453 and HCONT454 consist of 4 nodes connecting the HSHEAR353's end nodes, whereas the HCONT463 consists of 3 nodes where 2 nodes are HSHEAR353's end nodes and 1 node is to connect to the HSHEAR363's radial DOF. The contact element CONT152 was used to establish the contact between the bellmouth surface and the umbilical where the contact stiffness was set according to the above.

5.2. 3D local stress analysis models

The global model in Section 4 was further used and the elastic beam elements were replaced by the individual modeling of each helix and layer for the umbilical specimen. The principal umbilical cross section sketch is shown in Figure 2 where it is noted that the contact conditions for the tubes include both radial contact with core, fillers and sheath as well as hoop contact with the separation fillers. For the big tubes, deep grooves at the inner interface were observed giving a constraint with respect to motion in the lateral transverse direction. Therefore, two FE analyses were carried out to investigate different contacts and grooves effect on the stress behavior. The first FE analysis only included the radial contacts and was termed as "Radial contact model". The second analysis included both radial

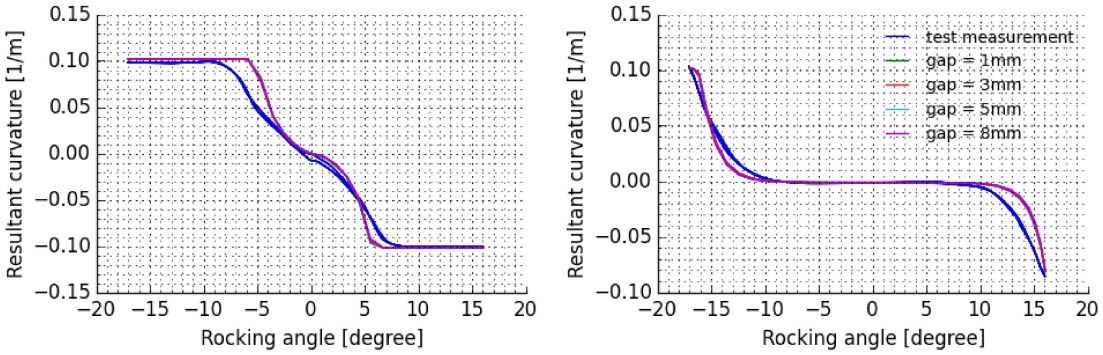

(a) Center tube at S2

(b) Center tube at S3

Figure 9: Sensitivity studies with respect to the gap between the bellmouth entrance and umbilical outer sheath under 200KN

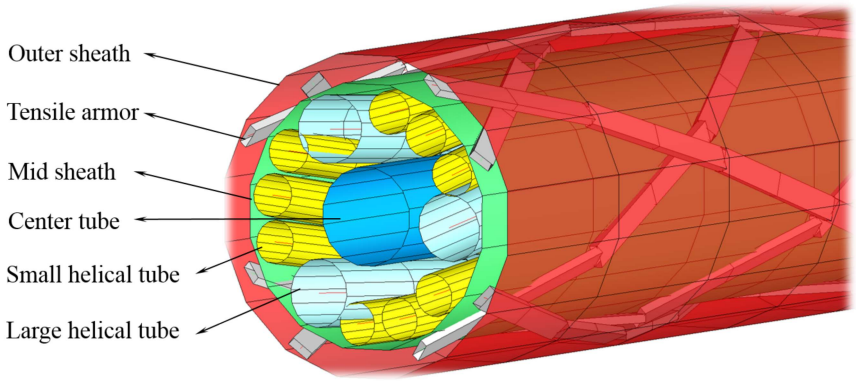

Figure 10: Modeling of each helix in the umbilical cross section in BFLEX

and hoop contacts. In addition, a spring element was attached to each element of the large tube in the transverse direction to include the groove constraint effect. It was termed as "Radial and constrained hoop contact model".

5.3. Penalty stiffness

The different fillers were found significantly deformed as shown in Figure 2, making it impossible to represent the real contact conditions based on ideal geometries as shown in Figure 3. Therefore, a simplified approach was introduced based on the following principles:

- Represent the contact stiffness based on the interface thickness and Young's modulus as well as the helix diameter. The modulus maintains the same value for all soft contacts.
- To ensure correct load sharing between the different helical elements, tune the modulus such that good correlation is obtained with the measured axial stiffness.

Realizing the complexity in the real contact conditions, a simplified contact stiffness model was applied:

$$K = \frac{ED}{t} \tag{13}$$

where E is the Young's modulus of the mid, inner sheaths and fillers, D is the tube's diameter and t is the thickness of supporting contact interface. The modulus E was 700MPa according to the manufacturer. The relevant parameters and associated contact stiffness of radial and hoop contact interfaces are shown in Table 2.

Two analyses were applied under a tension history 5-300KN by using the "Radial contact model" and "Radial and constrained hoop contact model" where the contact stiffness of each interface was set as shown in Table 2. This

aimed to investigate the contacts effect on the axial stiffness and verify the simplified method of setting the contact stiffness. Figure 11 presents the axial stiffness comparison results between the test measurement and two numerical analyses. The axial stiffness obtained by only including radial contacts is only 0.8% deviated from that obtained by including both radial and hoop contacts. This implies that the radial motion of steel tubes is not significantly influenced by the hoop contacts. It was also found that the axial stiffness obtained from numerical models correlated well with the test measurement. It was therefore concluded that the method of calculating the contact stiffness ensures correct load sharing of the internal components.

Table 2: Contact interfaces' thickness, steel tube diameter and contact stiffness data of radial and hoop contacts in the umbilical specimen cross section

Contact interface name	H_1-core	H_1-sheath	H_2-core	H_2-sheath	H_1-H_1	H_1-H_2
Thickness t [mm]	14	4	3	4	1	1
Diameter [mm]	15.3	15.3	27.4	27.4	15.3	21.35
Contact stiffness [MN/m^2]	765	2677	6393	4795	10710	14945

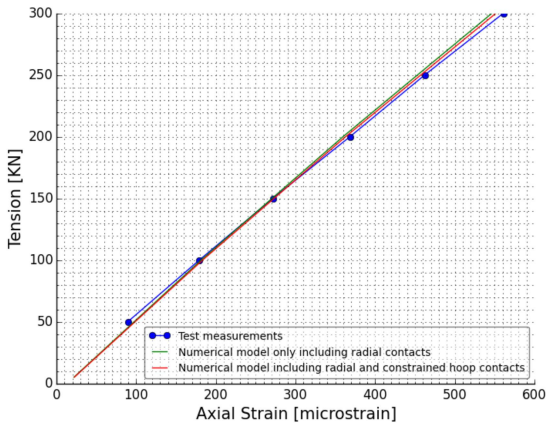

Figure 11: The umbilical's axial stiffness comparison results for validating the simplified method of calculating the contact stiffness.

5.4. Contact models effects on 2D assumption

It is noted in Figure 3 that the large and small tubes are located more close to the outermost fibre positions at S2. Therefore, all validation and comparison work in the following is carried out based on the stress behavior at S2. Figure 12 presents the dynamic axial strain behavior of large and small tubes in the full scale testing at S2. A significant hysteresis was formed because the internal friction acted to resist the reversed motion. A section of relatively constant strain range is found in the test measurement within small curvature range and was termed as "Coulomb friction strain range". The small curvature range normally governs the fatigue life. Therefore, it is important to correctly predict the Coulomb friction strain range. 2D local analysis is preferred to calculate the Coulomb friction strain when 3D effects are not significant. Various methods can be used to simulate 2D behavior. For example, the UFLEX2D and HELICA[25] softwares employ an analytical bending model to calculate friction force assuming harmonic motion of the helix. The extreme axial strain range at the outermost fibre position is obtained from integrating friction force distributed along twice a quarter of pitch length, which is given by:

$$\epsilon_F = \frac{\pi R \sum f^i}{EA_s sin\alpha} \tag{14}$$

where μ is friction coefficient, R is layer radius, α is the lay angle, EA_s is the large tube' axial stiffness and $\sum f^i$ is the sum of friction force of multiple contact interfaces. The friction force was calculated based on the Coulomb

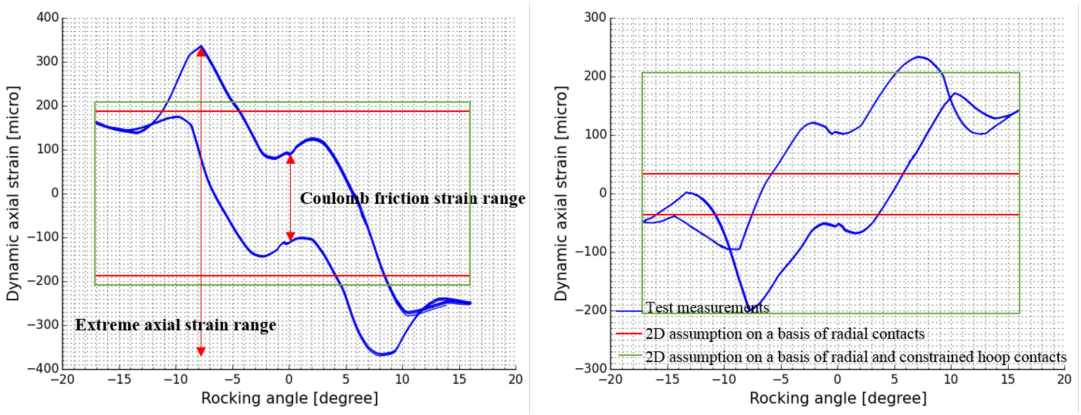

(a) Large tube (b) Small tube

Figure 12: The comparison results of large and small tubes with respect to dynamic axial strain behavior between the measurements and predicted values based on 2D assumption.

friction concept by applying constant friction coefficient and contact force. The contact force was then obtained either by only including radial contact interfaces or by including both radial and hoop contacts in numerical models.

Firstly, the "Radial contact model" was used by applying tension 200KN. The contact line force of each interface for two tubes were obtained as presented in Table 3. A friction coefficient of 0.2 was assumed. Table 4 summarizes the Coulomb friction strain ranges of two tubes obtained from the 2D assumption based on different contact models. It is seen that the Coulomb friction strain range of large and small tubes by only including radial contacts above were 87% overestimated and 55% underestimated, respectively.

Then, the "Radial and hoop contact model" was applied under tension 200KN. The corresponding contact line forces are shown in Table 3. It is found that the total contact line force was increased by 13% for the large tube by also including hoop contacts, resulting in the same increase in the Coulomb friction strain range as illustrated in Figure 12a. The total contact line force was increased by nearly a factor of 6 for the small tube, giving the same factor to the Coulomb friction strain range, see Table 4. The Coulomb friction strain ranges of two tubes were 112% and 162% overestimated. This confirms the importance of including hoop contacts when applying the 2D assumption. However, it is observed that the nonlinear axial strain history and the extreme values cannot be correctly described by a 2D assumption.

Table 3: Contact line force of large and small tubes in the "Radial contact model" as well as "Radial and hoop contact model" under tension 200KN

FE model name	Contact interface name	Contact line force of Large tube [N/m]	Contact line force of Small tube [N/m]
Radial contact model	tube-inner core	27000	6000
	tube-mid sheath	22000	2000
Radial and constrained hoop contact model	tube-inner core	4500	550
	tube-mid sheath	11000	6350
	small tube - large tube	20000	20000
	small tube - large tube or small tube - small tube	20000	20000

Table 4: Coulomb friction strain range obtained from 2D assumption based on differnt contact models

	Coulomb friction strain of large tube [microstrain]	Coulomb friction strain of small tube [microstrain]
Test measurements	200	158
2D assumption on a basis of radial contacts	374	70.4
2D assumption on a basis of radial and hoop contact contacts	424	414

5.5. 3D cyclic bending analysis

As both the extreme and Coulomb friction axial strain ranges cannot be correctly represented by the 2D assumption, 3D cyclic bending analyses were carried out by using the "Radial contact model" and "Radial and constrained hoop contact model" where the bellmouth was moved according to the full scale testing procedures under tension 200KN. This aimed to investigate the different contacts effect on the dynamic axial strain behavior. The friction model developed in Dai et al.' work[23, 24] was applied with shear interaction stick stiffness of 200 $[MN/m^2]$ and friction friction coefficient 0.2.

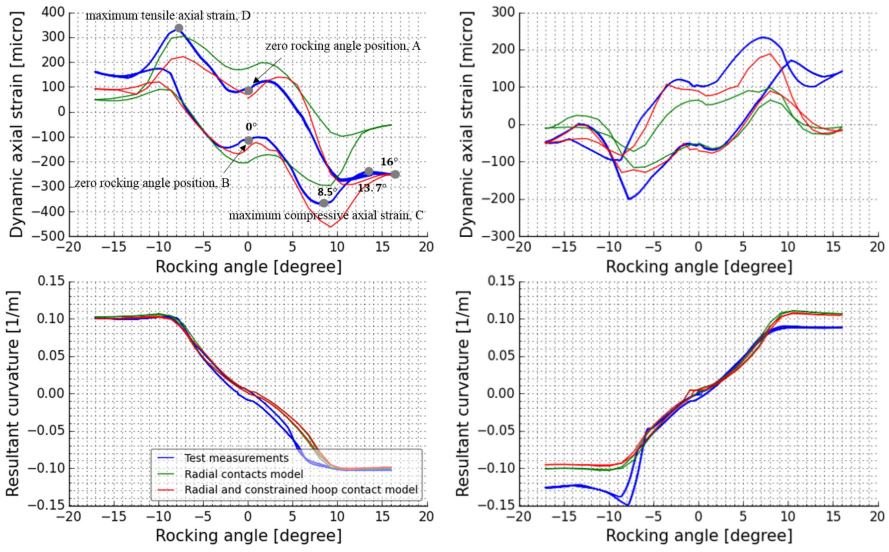

(a) Large tube at S2 (b) Small tube at S2

Figure 13: Large and small tubes' dynamic axial strain and resultant curvature correlation results between test measurements and two 3D FE models where the bellmouth was moved according to the full scale testing procedures under tension 200KN. The FE models include the "Radial contact model" and "Radial and constrained hoop contact model".

Figure 13 presents the numerical results of dynamic axial strain and resultant curvature at the cross section center of large and small tubes at S2 and test measurements. It is seen that the compressive axial strain significantly increased with increasing curvature until approaching the maximum value at rocking angle 8.5°, as denoted in Figure 13. Figure 14 presents the global curvature distribution along the umbilical length. Two pitches in the left and right sides of S2 are denoted as "pitch A" and "pitch B", respectively. Figure 15 shows the helices angular positions along the umbilical length in "pitch A" and "pitch B" for better understanding the friction behavior according to their locations. The curvature was found to be nonlinearly distributed in "pitch A" and "pitch B". This is because the element within the bellmouth surface starts to subsequently contact with the bellmouth surface from the entrance position. Figure 16 shows the friction force distributions of large tube. It is seen that a section of approximately 1.1m of the large tube in the "pitch A" is activated to slip at rocking angle=8.5° in the same direction. This means

that more than a quarter of pitch length friction force contributes to building up the maximum compressive axial strain, resulting in increasing the axial strain. At rocking angle 13.7°, the elements around the "neutral axis position A1" as seen in Figure 15 were found to be moved to the opposite direction, resulting in opposite friction direction. This contributes to reducing the length of mobilized friction having same direction, thus reducing the axial force. Figure 17 shows the dynamic axial strain distribution of large tube. It is found that the elements of "pitch B" governed the axial force at rocking angle=13.7° which was confirmed by the increased tensile axial strain of "pitch B". Therefore, the friction distribution of "pitch A" remained same, resulting in constant axial strain at S2 at the rocking angle=13.7°-16°. The small tube's axial strain behavior was observed to be the similar to the large tube behavior.

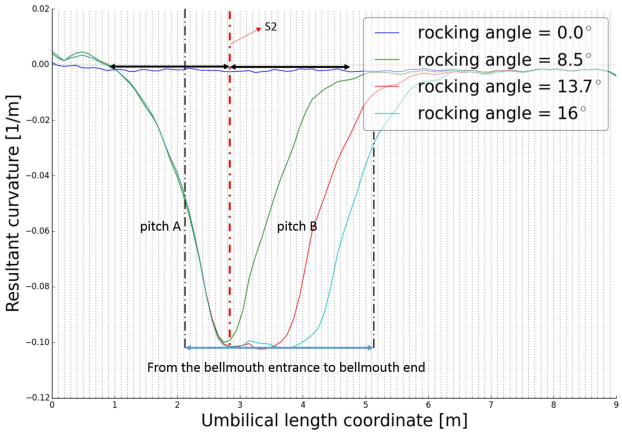

Figure 14: The global curvature distribution along the umbilical length

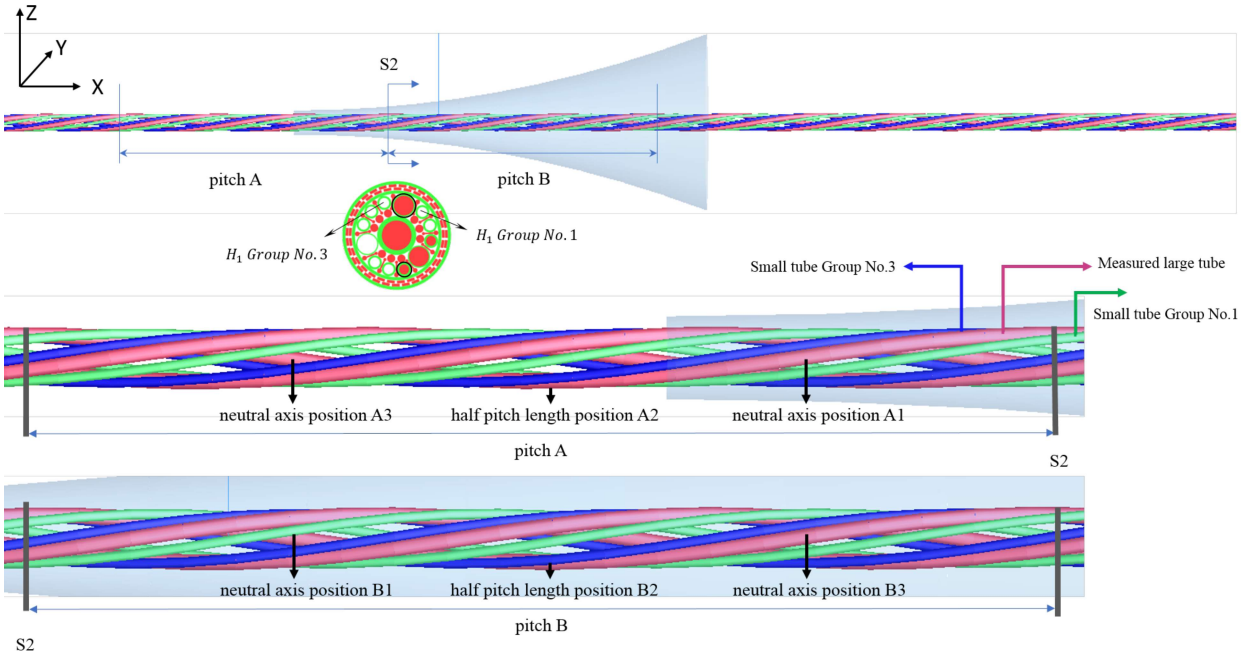

Figure 15: The 3D FE model for cyclic bending analysis

The Coulomb friction strain ranges of large and small tubes in "Radial contact model" were found similar to the values obtained by the 2D assumption when only including radial contacts, see Table 4 and 5. Figure 18 shows the

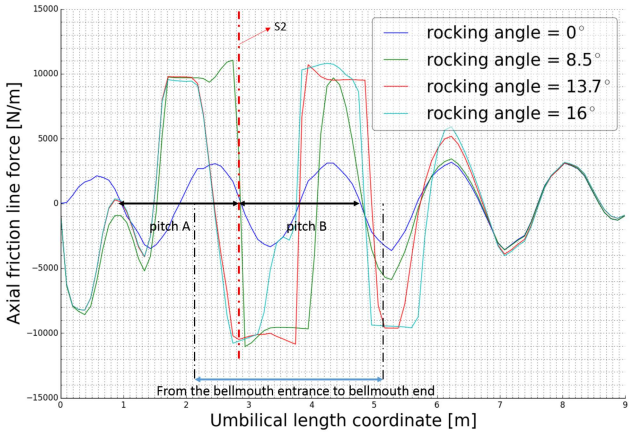

Figure 16: The friction line force distribution along the umbilical length for the contact interface between the large tube and mid sheath in the radial contact FE model.

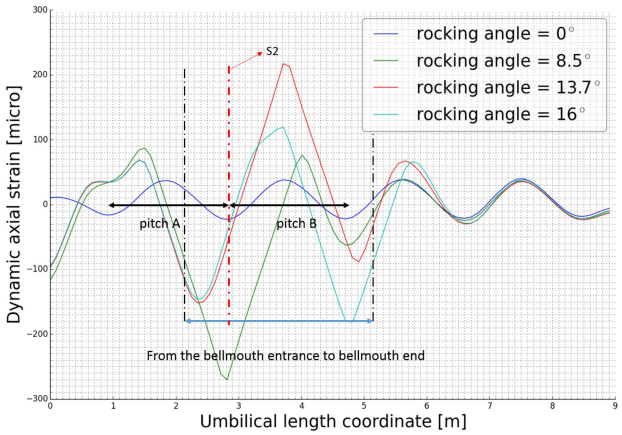

Figure 17: The dynamic axial strain distribution of large tube along the umbilical length

friction distribution of "Radial contact model" and "Radial and constrained hoop contact model" at zero rocking angle positions for the large tube. It is seen that friction force with same direction and constant amplitude of 10000 [N/m] is distributed along half pitch length in "pitch A". This implies that the same friction force is integrated along the same length to build up the Coulomb friction strain range in the "Radial contact model" as the 2D assumption by only including the radial contacts. Therefore, the same Coulomb friction strain range was obtained as the 2D assumption for the large tube. Similar friction effects were also found for the small tube.

However, the Coulomb friction strain ranges of large and small tubes in "Radial and constrained hoop model" was reduced and increased, respectively, by also including the hoop contacts. They were only 7.5% over and 0.4% under estimated as compared to the tests, see Table 5. Figure 19 shows the friction distribution of radial and hoop contact interfaces at zero rocking angle position A as shown in Figure 15. The measured large tube contacted with two small tubes, termed as "Group No.1" and "Group No.3", respectively, see Figure 15. A $\pi/2$ phase angle was observed between the friction distributions of radial and hoop contact interfaces, acting to reduce the friction amplitude as seen in Figure 18. Therefore, the friction force amplitude was reduced to an average of 4116 [N/m] with the same direction along half pitch length in "pitch A", resulting in a 44% decrease of the Coulomb friction strain range for the large tube. Similar friction effects were found for the small tube and Coulomb friction strain range at zero rocking angle position B. It was concluded that it is important to include hoop contacts in addition to the radial contacts for considering the phase effect.

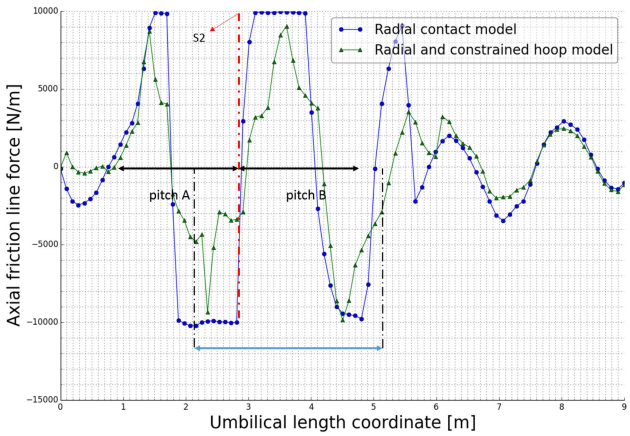

(a) At zero rocking angle position A

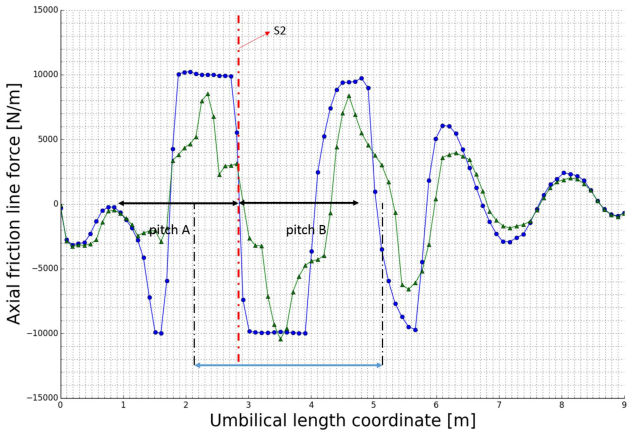

(b) At zero rocking angle position B

Figure 18: Friction force distributions of the large tube at zero rocking angle positions in the "Radial contact model" and "Radial constrained hoop contact model".

Table 5: The Coulomb friction strain range comparison between 2D assumption and 3D FE models based on diffrent contact models

	Coulomb friction strain of large tube [microstrain]	Coulomb friction strain of small tube [microstrain]
Test measurements	200	158
Radial contact model in BFLEX	386	115
Radial and constrained hoop contact model in BFLEX	215	151

Figure 20 shows the friction distributions of large tube in "Radial contact model" and "Radial and constrained hoop contact model" at maximum compressive and tensile axial strain positions C and D which are denoted in Figure 13. In "Radial contact model", the friction force with same direction was developed along 1.2m of large tube in "pitch A" contributing to the maximum compressive strain as seen in Figure 20a. It means that more than a quarter of pitch length of friction force was activated, resulting in building up larger maximum compressive axial strain than that obtained by the 2D assumption. Similar friction effect was also found for the maximum tensile axial strain. However, the extreme axial strain range was underestimated.

For the "Radial and constrained hoop contact model", the maximum compressive axial strain was significantly in-

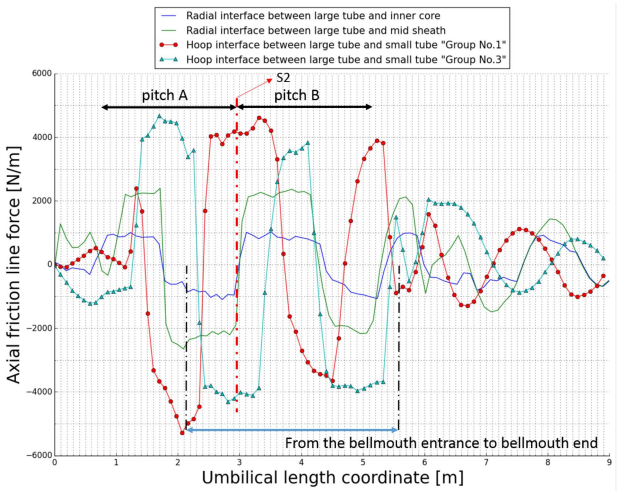

Figure 19: Friction force distribution of radial and hoop contact interfaces in "Radial and constrained contact model".

creased. In Figure 20a, the friction force of elements located from the neutral axis position A1 to S2 was larger than that of the "Radial contact model", resulting in increasing the slip capacity. Then more energy is governed by the elastic energy which is reflected by the significantly increased maximum compressive axial strain with less friction energy dissipation. The maximum tensile axial was reduced because shorter large tube had the same friction direction in "pitch A", as shown in Figure 20b. However, only 0.7% deviation was found with respect to the extreme axial strain range for the large tube. It was concluded that it is important to individually model each helix and include all contact interfaces in the 3D FE model as well as the local constraint effect in order to obtain the extreme value. For the small tube, the extreme axial strain range was underestimated by a 26% deviation.

A sensitivity analysis was carried out by using a friction factor of 0.25 for the "Radial and constrained hoop contact model". The results showed that the extreme axial strain ranges of large and small tubes were over and under estimated by 17% and 11.2%. This implies that the slip capacity is increased with increasing friction coefficient, resulting in more energy being governed by the elastic deformation. The Coulomb friction strain ranges of large and small tubes were 25% and 17% overestimated, respectively, due to the increased friction force.

The resultant curvature range of large tube correlated well with the tests. The measured curvature of small tube in tensile side is 22% larger than that of the bellmouth surface whereas it is 33% smaller in the compressive side, resulting in a total deviation of 12.5%. This might be due to local deformation effects that cannot be captured by the present contact model. However, the resultant curvature at both sides correlated well with the bellmouth surface curvature for both large and small tubes.

6. Conclusions and future work

- Full scale tests were carried out by mounting the fibre-optic braggs inside steel tubes of a 9m long umbilical specimen. The specimen was exposed to constant tension and dynamic curvature by means of two different bellmouth geometries of which one was focused on in the present work. The steel tubes' axial strain and local curvatures were measured. The tests results provided validation data for the local stress analysis where nonlinear effects were observed at extreme rocking angles.
- There existed some uncertain setup parameters including the gap between the bellmouth entrance and the outer sheath as well as the penalty stiffness needed in the contact element to represent the bellmouth geometry. It was found that the axial strain was not sensitive to the gap when the value was smaller than 8mm and a surface contact stiffness 100 $[MN/m^2]$ was found sufficient to describe the bellmouth surface.
- Realizing that the present umbilical cross section is too complex to model by a full 3D model, the strategy adopted in the present work was based on sandwich beam theory with dedicated curved beam elements and

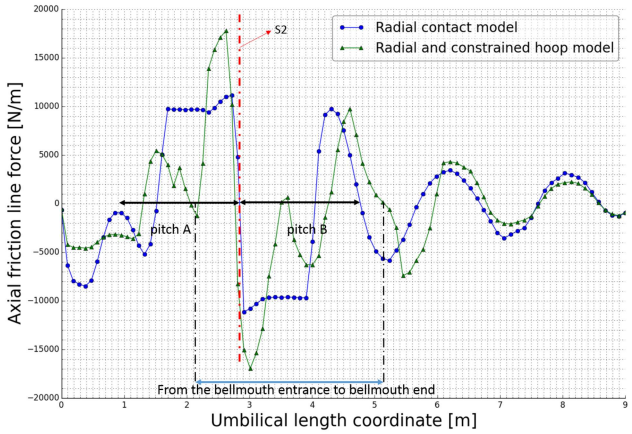

(a) At maximum compressive axial strain C

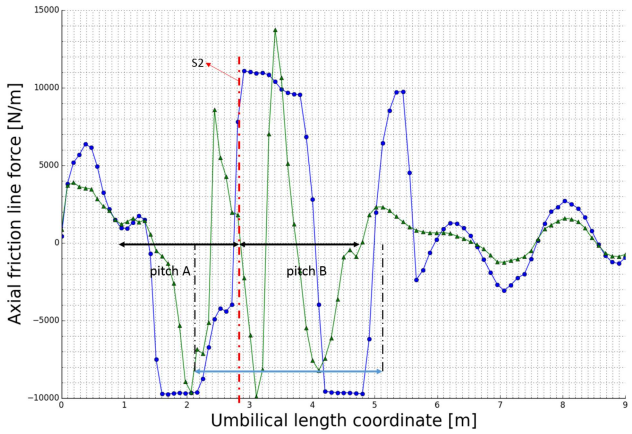

(b) At maximum tensile axial strain D

Figure 20: Friction force distributions of the large tube at maximum compressive and tensile axial strain positions in the "Radial contact model" and "Radial constrained hoop contact model".

associated penalty based contact elements. As hoop contacts existed between steel tubes and separation fillers, a tailor-made contact element was formulated to facilitate the hoop contacts. In addition, individual helix modeling was needed to capture 3D effects observed in the tests. However, it was observed that the fillers and sheath were severely deformed, making it impossible to represent the real contact stiffness based on the idealized cross section. Therefore, a simplified approach was proposed to determine the contact stiffness. It was determined by the interface thickness and Young's modulus as well as the helix diameter. Good correlation was obtained with respect to the axial stiffness, which verified the contact stiffness method to ensure the correct load sharing of internal components.

- As small curvature normally governs the fatigue life, it is important to correctly calculate the Coulomb friction strain range observed in the full scale tests. Two alternatives were used to calculate it by 2D assumption or 3D cyclic bending analysis. The Coulomb friction strain ranges of large and small tubes obtained based on 2D assumption were 87% over and 55% under estimated, respectively, when only including radial contacts. The ranges of large and small tubes were 112% and 162% overestimated by also including hoop contacts. This confirmed the importance of including all contact interfaces in the 2D assumption.

- 3D cyclic bending analyses were carried out by using the "Radial contact model" and "Radial and constrained hoop contact model" where the bellmouth was moved according to the full scale testing procedures under tension 200KN. The Coulomb friction strain range obtained in the "Radial contact model" was similar to the value in the 2D assumption by only including the radial contacts. However, the Coulomb friction strain ranges

of large and small tubes were reduced and increased and had good correlation with the tests by applying the hoop contacts. This was found to be due to a $\pi/2$ phase difference between the friction forces mobilized along the radial and hoop interfaces, acting to reduce the friction force to build up the axial strain. This will act to reduce the conservatism during fatigue calculations.

- The extreme axial strain range of large tube by only including radial contacts was underestimated, however, it correlated well with the tests by also including the constraint effect and hoop contacts. The constraint resulted in redistribution of radial and hoop contact forces and larger friction force distributed along the tube, which means that the full slip capacity was increased. Then more energy was governed by the elastic energy resulting in significantly increasing the deformation of large tube with less friction energy dissipation. These effects can only be described by 3D modeling of each helix which is the only possibility to obtain the correct extreme axial strain range.
- The resultant curvature range of large tube correlated well with the tests. For the small tube, it was deviating 12.5% as compared to the tests. This might be due to local deformation that cannot be captured in the present model.
- The contact stiffness calculated based on the simplified method was only validated for one umbilical specimen. Therefore, it will be beneficial to verify this method by more umbilical full scale testing with respect to axial stiffness.
- The same applies with respect to the dynamic stresses where more data is needed to verify the models specially for bending stiffener cases which govern the majority of flexible riser designs.
- The present contact elements do not include friction coupling between torsion and lateral motions. This should be improved in future work.

Acknowledgments

The authors would like to express our appreciations to Kristian Minde, Emil Bratlie, Nina Langhelle, Janne Kristin Økland Gjøsteen and Dag Fergestad at SINTEF Ocean for their help to understand the testing procedures in the Join Industry Project on Stress and Fatigue Analysis of Umbilicals, Phase II. Dr.Philippe Mainçon is much acknowledged for his help with respect to the test measurements treatment. We also thank the Umbilical JIP sponsors for permitting publishing this article.

Reference

[1] Svein Sævik. Bflex2010 theory manual. *SINTEF OCEAN*, 2010.

[2] Qianjin Yue, Qingzhen Lu, Jun Yan, Jiexin Zheng, and Andrew Palmer. Tension behavior prediction of flexible pipelines in shallow water. *Ocean Engineering*, 58:201–207, 2013.

[3] Rene Santos Almeida, Wesley Novaes Mascarenhas, Jose Fabio Abreu de Andrade, Antonio Fernando Abreu de Andrade, et al. Application of numerical analysis tools on the performance improvement of umbilicals and their elements. In *OTC Brasil*. Offshore Technology Conference, 2013.

[4] Qing-zhen Lu, Qian-jin Yue, Zhi-xun Yang, Gang Wang, Jun Yan, and Yan Qu. Cross-sectional layout analysis of steel tube umbilical. In *ASME 2012 31st International Conference on Ocean, Offshore and Arctic Engineering*, pages 493–497. American Society of Mechanical Engineers, 2012.

[5] Qingzhen Lu, Zhixun Yang, Jun Yan, and Qianjin Yue. Design of cross-sectional layout of steel tube umbilical. *Journal of Offshore Mechanics and Arctic Engineering*, 136(4):041401, 2014.

[6] Zhixun Yang, Qingzhen Lu, Jun Yan, Jinlong Chen, and Qianjin Yue. Multidisciplinary optimization design for the section layout of umbilicals based on intelligent algorithm. *Journal of Offshore Mechanics and Arctic Engineering*, 140(3):031702, 2018.

[7] AB Custódio and MA Vaz. A nonlinear formulation for the axisymmetric response of umbilical cables and flexible pipes. *Applied Ocean Research*, 24(1):21–29, 2002.

[8] Ian Probyn, Alan Dobson, Michael Martinez, et al. Advances in 3-d fea techniques for metallic tube umbilicals. In *The Seventeenth International Offshore and Polar Engineering Conference*. International Society of Offshore and Polar Engineers, 2007.

[9] Vincent Le Corre and Ian Probyn. Validation of a 3-dimensional finite element analysis model of deep water steel tube umbilical in combined tension and cyclic bending. In *ASME 2009 28th International Conference on Ocean, Offshore and Arctic Engineering*, pages 77–86. American Society of Mechanical Engineers, 2009.

[10] RH Knapp, Terry S Shimabukuro, et al. Structural analysis of composite umbilical cables. In *The Seventeenth International Offshore and Polar Engineering Conference*. International Society of Offshore and Polar Engineers, 2007.

[11] Alan Dobson and Dave Fogg. Fatigue testing and analysis of a deep water steel tube umbilical. In *ASME 2008 27th International Conference on Offshore Mechanics and Arctic Engineering*, pages 133–140. American Society of Mechanical Engineers, 2008.

[12] Ewan Brown et al. Steel tube umbilical design life verification by full-scale fatigue test. In *Offshore Technology Conference*. Offshore Technology Conference, 2011.

[13] Knut I Ekeberg, Mayuresh M Dhaigude, et al. Validation of the loxodromic bending assumption using high-quality stress measurements. In *The 26th International Ocean and Polar Engineering Conference*. International Society of Offshore and Polar Engineers, 2016.

[14] Mayuresh M Dhaigude, Knut I Ekeberg, et al. Validation of the loxodromic bending assumption using high-quality stress measurements–high tension case. In *The 26th International Ocean and Polar Engineering Conference*. International Society of Offshore and Polar Engineers, 2016.

[15] Howard Wang, C Blake Hebert, Gianluca Barbato, Lauro Silveira, Marco Vinicius dos Santos Paiva, Tiago B Coser, Facundo S López, Telmo R Strohaecker, Fabiano Bertoni, et al. Submarine power cable design validation through model testing. In *The 26th International Ocean and Polar Engineering Conference*. International Society of Offshore and Polar Engineers, 2016.

[16] Marco Vinicius dos Santos Paiva, Lauro Silveira, Howard Wang, C Blake Hebert, Tiago B Coser, Facundo S López, Telmo R Strohaecker, Fabiano Bertoni, et al. Validation of power cable local stress analysis. In *The 26th International Ocean and Polar Engineering Conference*. International Society of Offshore and Polar Engineers, 2016.

[17] Fergestad Dag, Janne Gjøsteen, and Philippe Mainçon. *Umbilical JIP-Phase II, full scale testing of specimen No.1*. SINTEF OCEAN, 2011.

[18] JK Gjøsteen and S Sævik. Expermiental validation of a 3-dimensional umbilical cross-section model. *International Conference on Floating Structures for Deepwater Operations*, pages 21–23, 2009.

[19] Svein Sævik. Bflex2010 user manual. *SINTEF OCEAN*, 2010.

[20] TY Chang, AF Saleeb, and SC Shyu. Finite element solutions of two-dimensional contact problems based on a consistent mixed formulation. *Computers & structures*, 27(4):455–466, 1987.

[21] SC Shyu, TY Chang, and AF Saleeb. Friction-contact analysis using a mixed finite element method. *Computers & structures*, 32(1):223–242, 1989.

[22] Svein Sævik. Uflex theory manual. *SINTEF OCEAN*, 2015.

[23] Tianjiao Dai, Svein Sævik, and Naiquan Ye. Friction models for evaluating dynamic stresses in non-bonded flexible risers. *Marine Structures*, 55:137–161, 2017.

[24] Tianjiao Dai, Svein Sævik, and Naiquan Ye. An anisotropic friction model in non-bonded flexible risers. *Marine Structures*, 59:423–443, 2018.

[25] Geir Skeie, Nils Sødahl, and Oddrun Steinkjer. Efficient fatigue analysis of helix elements in umbilicals and flexible risers: Theory and applications. *Journal of Applied Mathematics*, 2012, 2012.

Title: Experimental and numerical studies on dynamic stress and curvature in steel tube umbilicals

Authors: Tianjiao Dai[a], Svein Sævik[a] and Naiquan Ye[b]*

[a] Department of Marine Technology, Norwegian University of Science and Technology, NO-7491 Trondheim, Norway

[b] OIL and GAS, SINTEF OCEAN, Trondheim, NO-7052, Norway

Abstract

The present paper addresses the stresses in dynamic steel tube umbilicals at the platform hang-off exposed to large motions corresponding to an extreme storm condition. Experimental tests were carried out by mounting fibre-optic Braggs inside steel tubes of a 9m long umbilical specimen. Then the specimen was exposed to constant tension and dynamic curvature by means of a bellmouth and the stresses were measured. Realizing that the geometry of the umbilical cross section was too complex to apply full 3D modeling, a beam and penalty contact modeling procedure was applied to describe the extreme stress behavior. Then a simplified method was proposed to determine the contact stiffness which was further validated by full scale umbilical axial stiffness testing. As hoop contact interfaces between steel tubes and separation fillers were observed in the test specimen, a tailor-made contact element was formulated to facilitate hoop contact. Different modeling alternatives were used to investigate the hoop contact effect on the extreme axial stress and Coulomb friction stress range, which were further validated against measured dynamic axial stress. Good correlation was found by the combination of describing all contact interfaces and constraints due to the grooves in the inner sheath.

key words: umbilical, friction stress, axial stress, fatigue

1. Introduction

Subsea umbilicals have multiple functionalities in the subsea system application. They are mainly designed for subsea control and monitoring, chemical injection, fluid transportation, gas release and power transmission, etc. An umbilical consists of multiple groups of functional elements, such as electrical cables, optical fibre cables, hoses, steel tubes or fillers in the core, tensile armors for mechanical strength and ballast as well as the sheaths for protection and compactness. This determines several functional components in the cross section and involves different materials including metallic, extruded polymeric and fibres, etc. Due to multiple contacts between arbitrary components of different materials, stress analysis is very challenging with respect to accuracy, stability and computation time. The finite element method with full 3D modeling by solid finite element is the only alternative that can capture all nonlinearities in terms of geometry, material, end conditions and cross section arrangement, etc. However, this will result in a large number of degrees of freedom and long computation time. Further due to the contact between steel and plastic materials, for example, between steel and fillers, the large difference in material stiffness will introduce numerical instability issues. Noting that the longitudinal stress is the primary stress component of the helical elements, the strategy adopted in the present work has therefore been based on beam and beam penalty contact elements [1].

Several authors have investigated the cross section's internal stiffness capacity effect on the axial stress of helical components. Yue et al.[2] carried out tension tests for a flexible pipe and investigated the radial stiffness of the pressure armor effect on the tensile stiffness of the tensile armor layer. The decreased tensile stiffness was found with decreasing radial stiffness. Almeida et al.[3] did stress analyses of individual components in two different layout cross sections of umbilicals and a reduction 53% of hose stress was demonstrated when the free gap was considered between hoses and inner sheath. The internal stiffness capacity of an umbilical is normally less than that of a non-bonded flexible pipe due to the relatively soft core. Lu [4, 5] and Yang et al.[6] carried out finite element analyses of umbilicals for verifying the layout methodology considering nonlinear geometry, components compactness, materials and symmetry distribution by ensuring the contact pressure and radial displacement as small as possible. Custódio and Vaz [7] performed local axisymmetric analysis of non-bonded composite cables and pipes for considering the material and geometrical nonlinearities due to gap formation and lateral contact between wires. It was found that the radial contraction reduced the available gap between wires and the cable became stiffer when the wires touched together. Since the further radial contraction was constrained and the gap between two layers of wires may be increased, the contact pressure was reduced. It was found that the internal flexibility is directly determined by the components' motion, geometry, material and cross section arrangement, etc. Therefore, the beam contact models should be capable to capture these effects by formulating this behavior into the contact stiffness and beam kinematics.

There are few works reported concerning full scale measurements of the helical component's stress behavior. Probyn et al.[8, 9] performed tensile, bending and crush full scale tests and validated the 3D FEA analysis against the test results. Good correlations with respect to umbilical bending stiffness were obtained within elastic strain of steel tubes. However, the bending tests mainly focused on global bending moment and curvature history in a three points bending rig instead of measuring stress history of individual components. Knapp and Terry [10] emphasized that the radial deformation had an important effect on the axial strain as well as axial stiffness and good correlations were obtained in terms of axial strain and torque of the whole cable cross section under different tension levels between tests and the numerical model. Dobson et al.[11] reported a full scale test measuring individual steel tube by locating strain gauges at the steel tube's outer wall and the same strain gauge concept was applied in [12] where encouraging correlation between numerical model and test results of axial strain range for moderate prescribed curvatures was obtained. However, these tests were limited to measure each steel tube's local curvature. The local curvature was measured by locating two strain gauges in the inner wall of steel tubes and reported by Ekeberg and Dhaigude [13, 14]. In some power cable tests [15, 16], the tensile armors were instrumented with strain gauges through small windows on the outer sheath. A full scale test of a dynamic steel tube umbilical was carried out as part of the Umbilical JIP Phase II [17] in Marintek (SINTEF OCEAN, today) to measure the steel tube's axial strain and local curvature by post mounting four optic fibres in the steel tube's inner wall with 90° spacing in the circumferential direction. This test is used as a reference in the present work.

The objectives of the present work are summarized as follows:

1. Present the full scale tests [17, 18] carried out in SINTEF OCEAN and calculate the instrumented steel tubes' axial strain and local curvatures.
2. Perform the global numerical analyses for quantifying some test setup parameters including the gap between the bellmouth entrance and the specimen's outer sheath as well as the contact stiffness of the bellmouth surface, which are further applied in the local analysis.
3. Propose an analytical contact stiffness method for calculating contact stiffness of internal contact interfaces.
4. Propose a hoop contact element and implement it into the computer code BFLEX [1, 19].
5. Perform numerical analyses by using different modeling alternatives for investigating hoop contacts effect on the dynamic stress behavior and fatigue life prediction.

2. Experimental study

2.1. Test set-up

The test set-up is shown in Figure 1. It consisted of the umbilical specimen, adapter (extension piece for fitting the specimen to the load cell), rig components (rocking head, tower, bellmouth, tensioner actuator, logging system). The tower rig, specimen cross section and bellmouth are shown in Figure 2. The full scale umbilical specimen was delivered with two end fittings. The tensioner was used to apply constant tension at the specimen right end. Four tension levels were applied to the specimen, 5, 100, 200 and 300KN. Two bellmouths were fixed to the tower rig and rotated to apply bending loads to the umbilical. In the present work, only the second bellmouth with constant curvature 0.1 [1/m] was reported because the relatively large curvature may introduce significant nonlinear 3D effects on the helices when the specimen has full contact.

2.2. Specimen

A steel tube umbilical cross section is usually composed of functional components made of steel materials which are helically wound around a central core. The core may be a plastic or steel tube. Figure 3 presents the idealized geometry of the umbilical specimen at two measured sensor stations in this test. The cross section consisted of a main center tube, three large helical tubes, nine small helical tubes, twenty-one fillers, three sheath layers and two tensile armor layers, which were symmetrically arranged. The sheath over the center tube and fillers were used for separating direct contact between the large helical tube, center tube and small helical tubes. In addition, fillers were applied to fill out the interstitial voids between components for maintaining a compact and circular cross section. The helical tubes were wound together with the same lay angle, 7°. This bundle was over-sheathed by extruding an intermediate sheath. Two cross wound layers of tensile armors were arranged for avoiding substantial axial stress in the steel tubes. The tensile armors were covered by an outer sheath layer providing mechanical protection. The corresponding components' dimensions and radial locations are presented in Table 1.

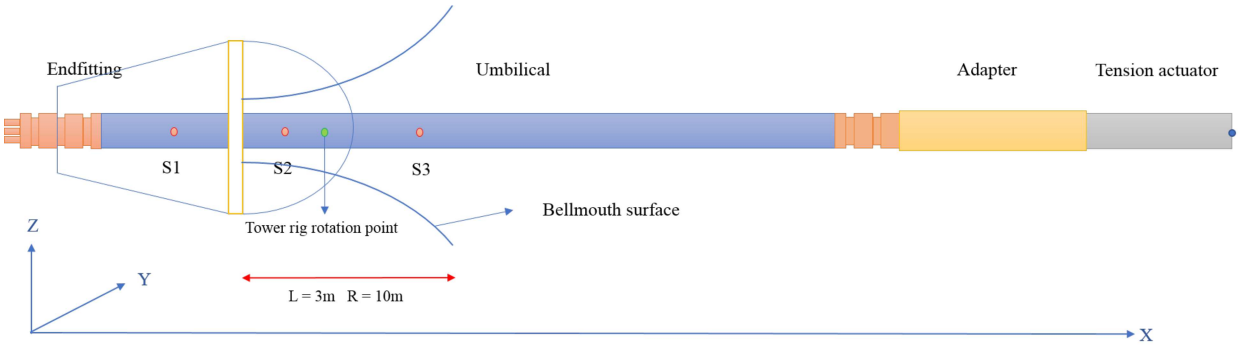

Figure 1: The test setup sketch

Tower rig | Specimen cross section | Specimen and bellmouth

Figure 2: The tower rig, specimen cross section and bellmouth in the full scale testing

Table 1: Components' dimension in the specimen cross section

Tube Name	Radial location [mm]	Outer diameter [mm]	Thickness [mm]	Pitch length [mm]
Center tube	0	44.1	3	1875
PE Inner sheath	0	50.1	3	–
Small tube	44.5	17.9	2.6	1875
Large tube	39.25	28.4	1.5	1875
Round polymeric filler	30.3	–	–	1875
Interstitial polymeric filler	44.3	–	–	1875
HDPE Mid sheath	0	55.45	4	–
Outer armor layer	63.62	–	3.5	1380
Inner armor layer	59.62	–	3.5	-775
HDPE Outer sheath	0	67.6	4	–

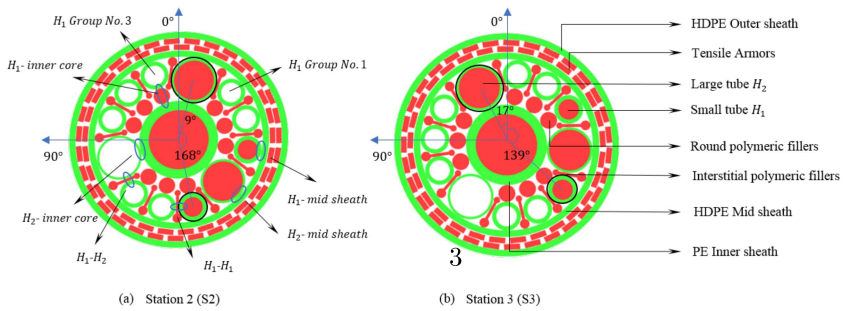

Figure 3: The cross sections at sensor station 2 (S2) and sensor station 3 (S3)

2.3. Optic fibre sensor stations

Three types of tubes were instrumented: the center tube, the large helical tube and the small helical tube. Three fibre bragg-grated (FBG) sensor stations were post mounted in the selected tubes by inserting steel bars where sensors were mounted. The sensor stations were then fixed to the inner wall by epoxy glue. The sensor station locations were selected according to the bellmouth length. The first station (abbreviated as S1) was positioned 0.95m away from the left end of umbilical and outside the bellmouth surface where small curvature was expected. The second station S2 was 0.675m away from the bellmouth entrance and the third station S3 was 0.352m away from the bellmouth end, see Figure 1.

Figure 4 presents the plastic spacing device which was used to mount four sensors and positioned parallel to its longitudinal axis. Then the local curvature of each instrumented tube can be obtained based on these four individual signals. Each optic fibre sensor should be located as far as possible from the tube center in order to guarantee the bending signals quality. The spacing device diameter was slightly less than the inner diameter of the corresponding instrumented tube to ease the post-installation.

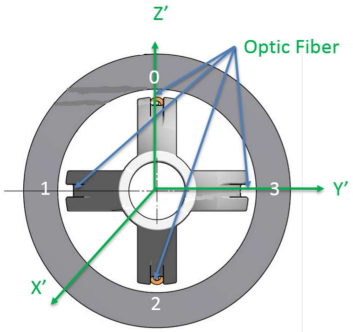

Figure 4: The spacing device for mounting the optic fibres

2.4. Post-processing of test data

The FBG is fabricated for reflecting a particular wavelength of light and transmitting all other ones. It is only constructed along a small segment of optic fibre at the sensor station. The strain of each optic fibre can be transformed from the change in wavelength due to the imposed strain. The axial strain at the center of the spacing device was calculated as the average of four strains from the optic fibres of each tube at each station. Additionally, the curvature around Y axis (κ'_y) and curvature around Z axis (κ'_z) of the spacing device can be obtained from the corresponding two opposite strain sensors seen in Eq. 2 and Eq. 3, respectively. Since the spacing device was post-mounted at each sensor station and fixed by epoxy, there had to be sufficient tolerance margins between the spacing devices and tubes' inner wall, resulting in eccentricities between the spacing device center and tube center. These eccentricities can be measured on the cross section by the specimen dissection. Therefore, the axial strain of tube in the center should be corrected based on the eccentricities and curvatures, given by Eq. 4.

Numerical studies were carried out in BFLEX, see Section 5. Figure 5 presents the global coordinate system of the test setup, the local coordinate system of tubes, and the spacing device coordinate system which are illustrated by the yellow, red and green colors, respectively. In order to be consistent with the local coordinate system defined in BFLEX, the curvatures measured in the spacing device coordinate system had to be transformed to the local coordinate system of the tube based on the measured angles between these two coordinate systems in the cross section after dissection. The curvatures in local system were obtained by the curvatures in the spacing device coordinate system and the transformation tensor as shown in Eq. 5.

The axial strain and curvature of tube in spacing device coordinate system are calculated as below:

$$\epsilon'_a = \frac{\epsilon'_0 + \epsilon'_1 + \epsilon'_2 + \epsilon'_3}{4} \tag{1}$$

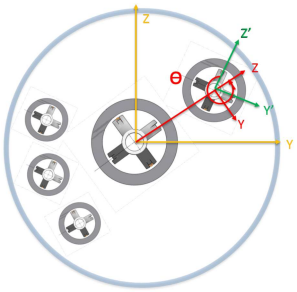

Figure 5: Global coordinate system of umbilical, local coordinate system of tube and coordinate system of spacing device

$$\kappa_y' = \frac{\epsilon_0' - \epsilon_2'}{z_0' - z_2'} \tag{2}$$

$$\kappa_z' = \frac{\epsilon_1' - \epsilon_3'}{y_3' - y_1'} \tag{3}$$

The axial strain and curvature of tube in the local coordinate system is shown in the following:

$$\epsilon_a = \epsilon_a' - (\kappa_y' z_e - \kappa_z' y_e) \tag{4}$$

$$\begin{bmatrix} \cos\theta & \sin\theta \\ -\sin\theta & \cos\theta \end{bmatrix} \begin{bmatrix} \kappa_z' \\ \kappa_y' \end{bmatrix} = \begin{bmatrix} \kappa_z \\ \kappa_y \end{bmatrix} \tag{5}$$

Where y_e and z_e are eccentricities between center of spacing device coordinate system and local coordinate system of the tube, θ is the angle rotated from spacing device coordinate system to local coordinate system.

3. Hoop contact model

As the hoop contacts were observed between the steel tubes and separation fillers in Figure 3, the hoop contact element was tailor-made and implemented into BFLEX and the HCONT454 element as shown in Figure 6. The method outlined in [20, 21] was used which is based on the concept of an Incremental Potential for including the constraint conditions between two bodies in contact. Referring to a Cartesian coordinate system, $x_i, i = 1, 2, 3$, the energy functional $\Delta\pi$ includes both terms related to the bodies A and B alone and terms associated with the contact conditions:

$$\Delta\pi = \sum_{l=A}^{B} \Delta\overline{\pi}^l - \int_{S_C} (\lambda_n + \Delta\lambda_n) \cdot g ds - \frac{1}{2\alpha_C} \int_{S_C} \Delta\lambda_n^2 ds - \int_{S_C} \lambda_t \cdot \Delta\gamma ds - \frac{1}{2} \int_{S_C} \Delta\lambda_t \Delta\gamma ds \tag{6}$$

Where $\Delta\pi^l$ is the incremental potential of bodies A and B alone, λ_n is the contact pressure and λ_t is the shear stress acting on the contact surface S_c. λ_t has to be based on the constitutive relation established related to friction. α_C is a scaling parameter related to the contact stiffness, assuming that the surface behaves elastic. g is the gap and γ is the tangential relative displacement.

For the two bodies to be in equilibrium at any instant within a time interval $[t, t + \Delta t]$, it is necessary to require:

$$\delta\Delta\pi = 0 \tag{7}$$

By carrying out the above variational procedure, the following constraint condition is recovered in addition to the traditional Euler equations and boundary conditions:

$$(\Delta \boldsymbol{u}_B - \Delta \boldsymbol{u}_A) \cdot \boldsymbol{n} + g_0 = \frac{\Delta\lambda_n}{\alpha_C} \tag{8}$$

Eq.8 represents a weak condition and the exact contact condition can only be recovered if $\alpha_C \to \infty$. Then for a given α_C, Eq.8 can be used to define the unknown contact pressure λ_n. The initial gap g_0 in the local helix X^2 direction at the time $t = 0$ can be approximated by:

$$g_0 = b(\frac{1}{F_f} - 1) \tag{9}$$

where b is the helix width and F_f is the layer fill factor defined by $F_f = \frac{nb}{\cos\alpha 2\pi R}$ where n is the number of helices in the same layer, α is the lay angle and R is the layer radius. Then the gap increment between t and $t + \Delta t$ is influenced by the incremental transverse displacement, radial and bending motions as:

$$g = \Delta u_2^B - \Delta u_2^A + \frac{b}{F_f}(\Delta\varepsilon_\psi + \Delta\varepsilon_{Z^1}) + g_0 \tag{10}$$

$\Delta\varepsilon_\psi$ is the hoop strain taken to be:

$$\Delta\varepsilon_\psi = \frac{1}{2R}(\Delta u_3^B + \Delta u_3^A) \tag{11}$$

$\Delta\varepsilon_{Z^1}$ is obtained from the supporting pipe global curvature as:

$$\Delta\varepsilon_{Z^1} = -Rsin\psi\Delta v_{,11} + Rcos\psi\Delta w_{,11} \tag{12}$$

where v and w are the transverse motion displacements of the umbilical center, see Figure 6. $_{,11}$ denotes differentiation with respect to the longitudinal pipe centerline coordinate Z^1, see Figure 7.

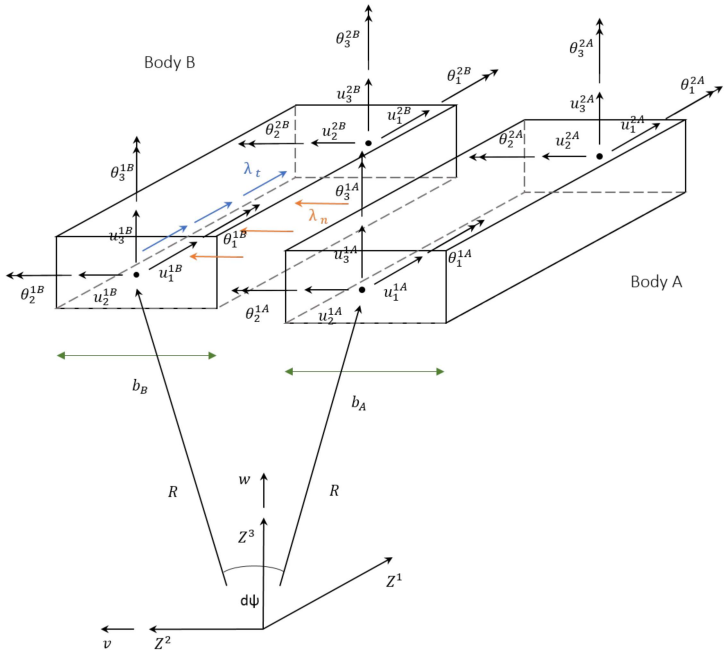

Figure 6: Hoop contact element HCONT454

4. Global analysis

Global analyses were carried out to evaluate the uncertain parameters in the test setup and verify the bellmouth geometry model in BFLEX. Figure 8 presents the global model consisting of umbilical, end fitting, load cell, adapter, tension actuator and bellmouth represented by the green surface. The full contacts between bellmouth surface and specimen in the tests are shown in Figure 8b and 8c. All parts were modeled by 354 elastic beam elements. The mechanical properties of the umbilical was obtained from UFLEX [22] by modeling each component in the cross section.

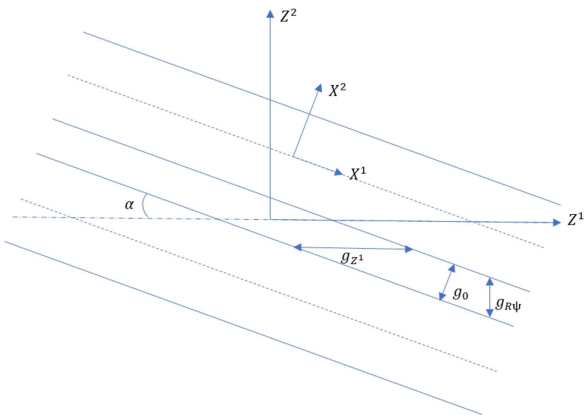

Figure 7: The gap definition in the hoop direction for the hoop contact element HCONT454

The end fitting, load cell and adapter elements were modeled by associating the elements with large axial, bending and torsion stiffnesses. The weight of these components were set to zero due to the weight compensating procedures applied in the test. The tensioner was free to rotate and the bending loads induced longitudinal displacement of the specimen was compensated by the tensioner elongation. Therefore, constant tension was recorded in all load cases in the tests. This physical property was achieved by modeling the beam element with small axial stiffness and applying the initial strain concept to obtain constant tension. The tension 200KN and self-weight of umbilical were applied before moving the bellmouth according to the full scale test procedure. A rigid link was established between the first umbilical element and the pivot point to simulate the rigid tower head by the element eccentricity.

The bellmouth geometry was generated based on a given curvature and length. The contact between the bellmouth surface and the umbilical was handled by the penalty based beam to surface contact element HCONT152 with a sufficient contact stiffness to obtain correct curvature without convergence problems. A sensitivity study was then carried out to determine this contact stiffness. It was found that as long as the stiffness is larger than 1E8 $[N/m^2]$, good correlation with the bellmouth surface curvature was obtained. The value of 1E8 was therefore used in following simulations.

In addition, the gap between the bellmouth entrance and the outer sheath should also be determined in the global analysis, since it was not measured in the test. As the gap was in an order of 5mm, a sensitivity study with respect to the gap was performed where the gap was set to be 1, 3, 5 and 8mm. Figure 9 presents comparison results between the center tube's curvature in the tests and umbilical global curvature obtained from simulations at S2 and S3 under tension 200KN. It is noted that the curvatures at two stations were not sensitive to the gap as long as the gap is smaller than 8mm. A gap equal to 3mm was then used in the local stress analyses. It was also found that the specimen curvature increased with rocking angle until about 7° and then maintained constant. This implies that the specimen starts to fully contact with the bellmouth surface at 7° and stays on the surface afterwards. Since the tension 200KN is sufficient to ensure full contact between the bellmouth and specimen, the value was further used in the 3D local stress analyses.

5. 3D Local stress analysis

5.1. Specimen cross section model

As there existed significant 3D effects in the tests including end effects, nonlinear and time-varying curvature distribution along the pipe, modeling of each helix over the full length was needed. In addition, the cross section is complex including multiple contact interfaces between different materials. The sandwich beam theory together with the penalty contact method was therefore adopted in the present work. Then 3D FE models were established to simulate the full scale testing in BFLEX. Figure 10 shows the individual modeling of each helix in the umbilical specimen cross section. The cross section parameters are presented in Table 1. Each component was modeled as an individual part except the fillers. The tensile wires and steel tubes were modeled by the curved beam element HSHEAR353 [1, 19]. The outer and intermediate sheathes were modeled by the HSHEAR363 element. This is a thin

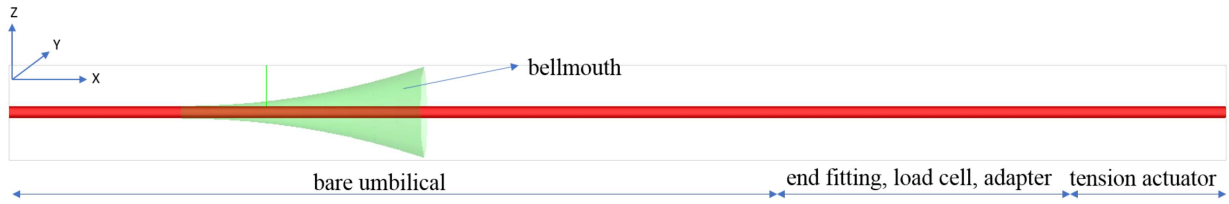

(a) Global model of full scale testing in BFLEX

(b) The umbilical has full contact with upper surface of bellmouth

(c) The umbilical has full contact with lower surface of bellmouth

Figure 8: Global model of full scale testing in BFLEX and the full contact condition between umbilical and bellmouth surface

shell/beam element including 3 nodes where 2 nodes (12 DOFs) are associated to the standard beam element which enables modeling torsion, bending and axial behavior of the sheath layers and 1 node (1 DOF) is used to describe the shell radial motion by means of the thin shell theory and the two dimensional version of Hooke's law. Based on mesh sensitivity study, the umbilical section was divided into 90 segments.

Since all functional components including tensile armors and steel tubes were modeled by beam elements, the interaction surfaces were modeled by penalty line contact elements to describe the inherent flexibility between components. The contact elements operate in the local surface system and include eccentricities, contact stiffness and friction effects, which calculate the contact line force and the friction by alternative friction models. The detailed features of curved beam and line contact elements have been described previously and are not repeated here, see [23, 24]. However, a brief summary of the modeling is given. The purpose of HCONT453 and HCONT454 are to describe radial and hoop contacts between two helical elements modeled by HSHEAR353. Since a beam element approach is adopted, local deformations due to filler contact needs to be built-into the penalty parameter of the contact element. HCONT463 element is used to establish the contact between the concentric layers modeled by HSHEAR363 and the helical element modeled by HSHEAR353. The HCONT453 and HCONT454 consist of 4 nodes connecting the HSHEAR353's end nodes, whereas the HCONT463 consists of 3 nodes where 2 nodes are HSHEAR353's end nodes and 1 node is to connect to the HSHEAR363's radial DOF. The contact element CONT152 was used to establish the contact between the bellmouth surface and the umbilical where the contact stiffness was set according to the above.

5.2. 3D local stress analysis models

The global model in Section 4 was further used and the elastic beam elements were replaced by the individual modeling of each helix and layer for the umbilical specimen. The principal umbilical cross section sketch is shown in Figure 2 where it is noted that the contact conditions for the tubes include both radial contact with core, fillers and sheath as well as hoop contact with the separation fillers. For the big tubes, deep grooves at the inner interface were observed giving a constraint with respect to motion in the lateral transverse direction. Therefore, two FE analyses were carried out to investigate different contacts and grooves effect on the stress behavior. The first FE analysis only included the radial contacts and was termed as "Radial contact model". The second analysis included both radial

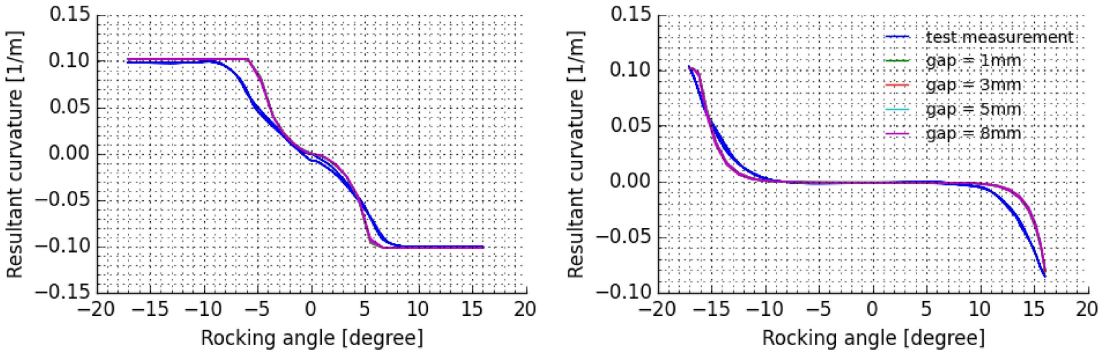

(a) Center tube at S2

(b) Center tube at S3

Figure 9: Sensitivity studies with respect to the gap between the bellmouth entrance and umbilical outer sheath under 200KN

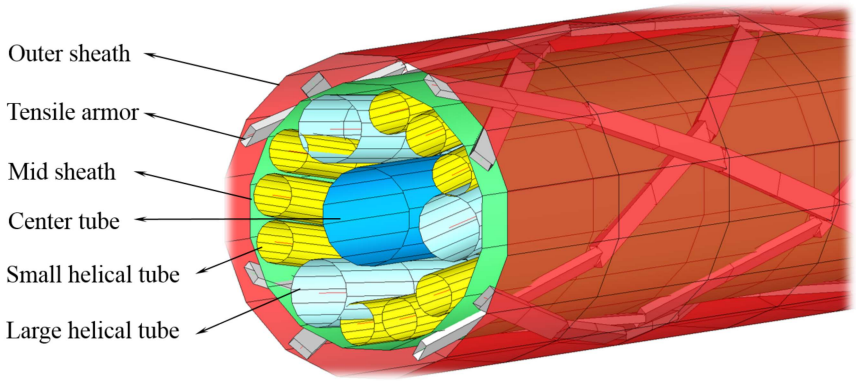

Figure 10: Modeling of each helix in the umbilical cross section in BFLEX

and hoop contacts. In addition, a spring element was attached to each element of the large tube in the transverse direction to include the groove constraint effect. It was termed as "Radial and constrained hoop contact model".

5.3. Penalty stiffness

The different fillers were found significantly deformed as shown in Figure 2, making it impossible to represent the real contact conditions based on ideal geometries as shown in Figure 3. Therefore, a simplified approach was introduced based on the following principles:

- Represent the contact stiffness based on the interface thickness and Young's modulus as well as the helix diameter. The modulus maintains the same value for all soft contacts.
- To ensure correct load sharing between the different helical elements, tune the modulus such that good correlation is obtained with the measured axial stiffness.

Realizing the complexity in the real contact conditions, a simplified contact stiffness model was applied:

$$K = \frac{ED}{t} \tag{13}$$

where E is the Young's modulus of the mid, inner sheaths and fillers, D is the tube's diameter and t is the thickness of supporting contact interface. The modulus E was 700MPa according to the manufacturer. The relevant parameters and associated contact stiffness of radial and hoop contact interfaces are shown in Table 2.

Two analyses were applied under a tension history 5-300KN by using the "Radial contact model" and "Radial and constrained hoop contact model" where the contact stiffness of each interface was set as shown in Table 2. This

aimed to investigate the contacts effect on the axial stiffness and verify the simplified method of setting the contact stiffness. Figure 11 presents the axial stiffness comparison results between the test measurement and two numerical analyses. The axial stiffness obtained by only including radial contacts is only 0.8% deviated from that obtained by including both radial and hoop contacts. This implies that the radial motion of steel tubes is not significantly influenced by the hoop contacts. It was also found that the axial stiffness obtained from numerical models correlated well with the test measurement. It was therefore concluded that the method of calculating the contact stiffness ensures correct load sharing of the internal components.

Table 2: Contact interfaces' thickness, steel tube diameter and contact stiffness data of radial and hoop contacts in the umbilical specimen cross section

Contact interface name	H_1-core	H_1-sheath	H_2-core	H_2-sheath	H_1-H_1	H_1-H_2
Thickness t [mm]	14	4	3	4	1	1
Diameter [mm]	15.3	15.3	27.4	27.4	15.3	21.35
Contact stiffness [MN/m^2]	765	2677	6393	4795	10710	14945

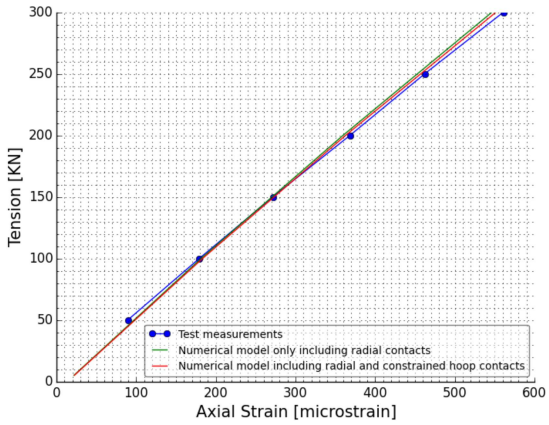

Figure 11: The umbilical's axial stiffness comparison results for validating the simplified method of calculating the contact stiffness.

5.4. Contact models effects on 2D assumption

It is noted in Figure 3 that the large and small tubes are located more close to the outermost fibre positions at S2. Therefore, all validation and comparison work in the following is carried out based on the stress behavior at S2. Figure 12 presents the dynamic axial strain behavior of large and small tubes in the full scale testing at S2. A significant hysteresis was formed because the internal friction acted to resist the reversed motion. A section of relatively constant strain range is found in the test measurement within small curvature range and was termed as "Coulomb friction strain range". The small curvature range normally governs the fatigue life. Therefore, it is important to correctly predict the Coulomb friction strain range. 2D local analysis is preferred to calculate the Coulomb friction strain when 3D effects are not significant. Various methods can be used to simulate 2D behavior. For example, the UFLEX2D and HELICA[25] softwares employ an analytical bending model to calculate friction force assuming harmonic motion of the helix. The extreme axial strain range at the outermost fibre position is obtained from integrating friction force distributed along twice a quarter of pitch length, which is given by:

$$\epsilon_F = \frac{\pi R \sum f^i}{EA_s sin\alpha} \tag{14}$$

where μ is friction coefficient, R is layer radius, α is the lay angle, EA_s is the large tube' axial stiffness and $\sum f^i$ is the sum of friction force of multiple contact interfaces. The friction force was calculated based on the Coulomb friction concept by applying constant friction coefficient and contact force. The contact force was then obtained

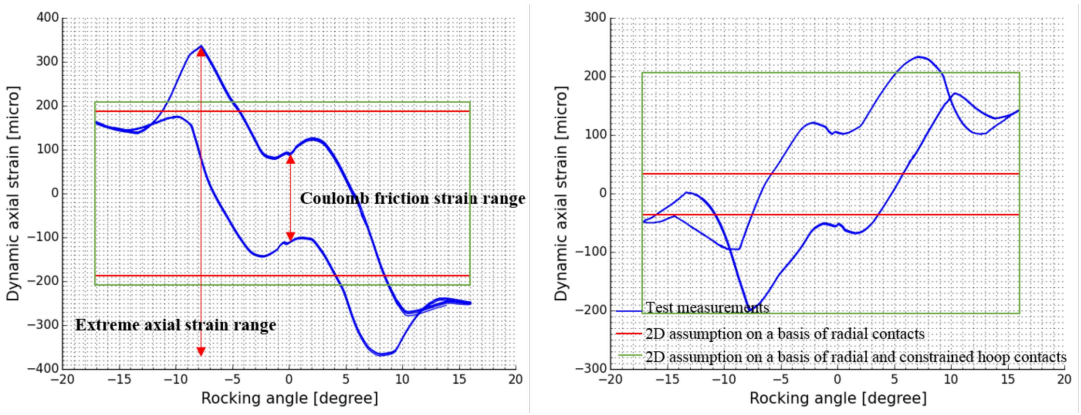

(a) Large tube (b) Small tube

Figure 12: The comparison results of large and small tubes with respect to dynamic axial strain behavior between the measurements and predicted values based on 2D assumption.

either by only including radial contact interfaces or by including both radial and hoop contacts in numerical models.

Firstly, the "Radial contact model" was used by applying tension 200KN. The contact line force of each interface for two tubes were obtained as presented in Table 3. A friction coefficient of 0.2 was assumed. Table 4 summarizes the Coulomb friction strain ranges of two tubes obtained from the 2D assumption based on different contact models. It is seen that the Coulomb friction strain range of large and small tubes by only including radial contacts above were 87% overestimated and 55% underestimated, respectively.

Then, the "Radial and hoop contact model" was applied under tension 200KN. The corresponding contact line forces are shown in Table 3. It is found that the total contact line force was increased by 13% for the large tube by also including hoop contacts, resulting in the same increase in the Coulomb friction strain range as illustrated in Figure 12a. The total contact line force was increased by nearly a factor of 6 for the small tube, giving the same factor to the Coulomb friction strain range, see Table 4. The Coulomb friction strain ranges of two tubes were 112% and 162% overestimated. This confirms the importance of including hoop contacts when applying the 2D assumption. However, it is observed that the nonlinear axial strain history and the extreme values cannot be correctly described by a 2D assumption.

Table 3: Contact line force of large and small tubes in the "Radial contact model" as well as "Radial and hoop contact model" under tension 200KN

FE model name	Contact interface name	Contact line force of Large tube [N/m]	Contact line force of Small tube [N/m]
Radial contact model	tube-inner core	27000	6000
	tube-mid sheath	22000	2000
Radial and constrained hoop contact model	tube-inner core	4500	550
	tube-mid sheath	11000	6350
	small tube - large tube	20000	20000
	small tube - large tube or small tube - small tube	20000	20000

Table 4: Coulomb friction strain range obtained from 2D assumption based on different contact models

	Coulomb friction strain of large tube [microstrain]	Coulomb friction strain of small tube [microstrain]
Test measurements	200	158
2D assumption on a basis of radial contacts	374	70.4
2D assumption on a basis of radial and hoop contact contacts	424	414

5.5. 3D cyclic bending analysis

As both the extreme and Coulomb friction axial strain ranges cannot be correctly represented by the 2D assumption, 3D cyclic bending analyses were carried out by using the "Radial contact model" and "Radial and constrained hoop contact model" where the bellmouth was moved according to the full scale testing procedures under tension 200KN. This aimed to investigate the different contacts effect on the dynamic axial strain behavior. The friction model developed in Dai et al.' work[23, 24] was applied with shear interaction stick stiffness of 200 $[MN/m^2]$ and friction friction coefficient 0.2.

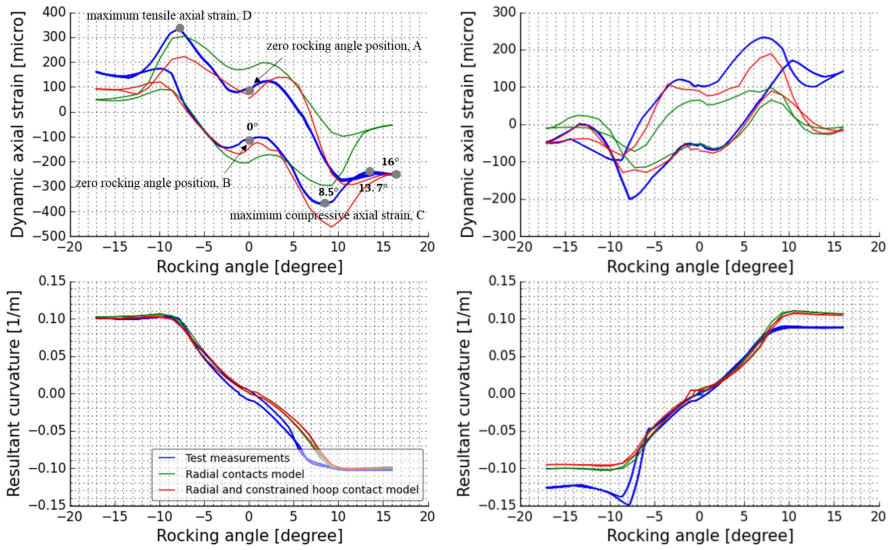

(a) Large tube at S2 (b) Small tube at S2

Figure 13: Large and small tubes' dynamic axial strain and resultant curvature correlation results between test measurements and two 3D FE models where the bellmouth was moved according to the full scale testing procedures under tension 200KN. The FE models include the "Radial contact model" and "Radial and constrained hoop contact model".

Figure 13 presents the numerical results of dynamic axial strain and resultant curvature at the cross section center of large and small tubes at S2 and test measurements. It is seen that the compressive axial strain significantly increased with increasing curvature until approaching the maximum value at rocking angle 8.5°, as denoted in Figure 13. Figure 14 presents the global curvature distribution along the umbilical length. Two pitches in the left and right sides of S2 are denoted as "pitch A" and "pitch B", respectively. Figure 15 shows the helices angular positions along the umbilical length in "pitch A" and "pitch B" for better understanding the friction behavior according to their locations. The curvature was found to be nonlinearly distributed in "pitch A" and "pitch B". This is because the element within the bellmouth surface starts to subsequently contact with the bellmouth surface from the entrance position. Figure 16 shows the friction force distributions of large tube. It is seen that a section of approximately 1.1m of the large tube in the "pitch A" is activated to slip at rocking angle=8.5° in the same direction. This means

that more than a quarter of pitch length friction force contributes to building up the maximum compressive axial strain, resulting in increasing the axial strain. At rocking angle 13.7°, the elements around the "neutral axis position A1" as seen in Figure 15 were found to be moved to the opposite direction, resulting in opposite friction direction. This contributes to reducing the length of mobilized friction having same direction, thus reducing the axial force. Figure 17 shows the dynamic axial strain distribution of large tube. It is found that the elements of "pitch B" governed the axial force at rocking angle=13.7° which was confirmed by the increased tensile axial strain of "pitch B". Therefore, the friction distribution of "pitch A" remained same, resulting in constant axial strain at S2 at the rocking angle=13.7°-16°. The small tube's axial strain behavior was observed to be the similar to the large tube behavior.

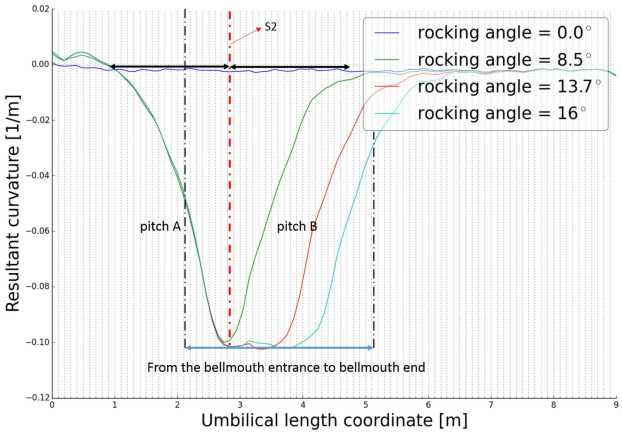

Figure 14: The global curvature distribution along the umbilical length

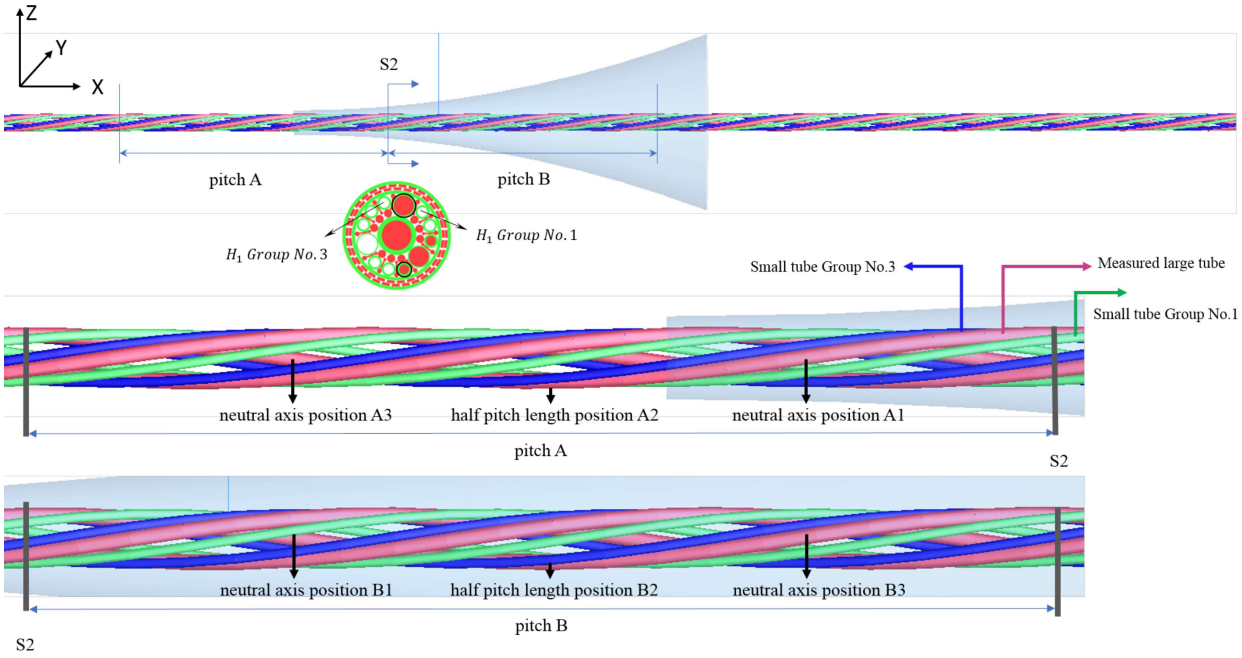

Figure 15: The 3D FE model for cyclic bending analysis

The Coulomb friction strain ranges of large and small tubes in "Radial contact model" were found similar to the values obtained by the 2D assumption when only including radial contacts, see Table 4 and 5. Figure 18 shows the

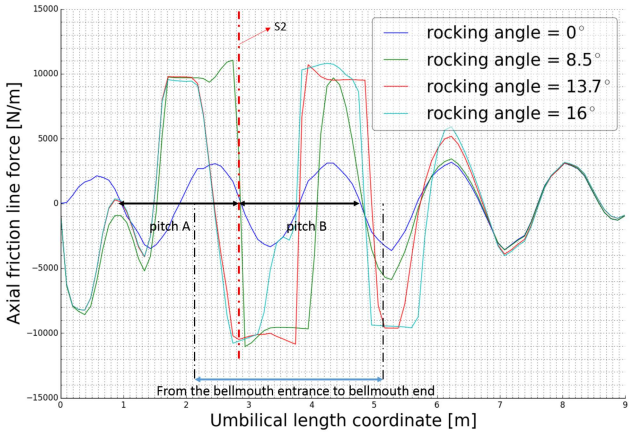

Figure 16: The friction line force distribution along the umbilical length for the contact interface between the large tube and mid sheath in the radial contact FE model.

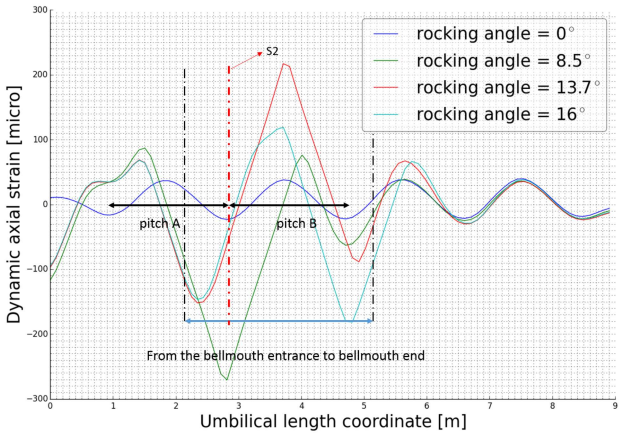

Figure 17: The dynamic axial strain distribution of large tube along the umbilical length

friction distribution of "Radial contact model" and "Radial and constrained hoop contact model" at zero rocking angle positions for the large tube. It is seen that friction force with same direction and constant amplitude of 10000 [N/m] is distributed along half pitch length in "pitch A". This implies that the same friction force is integrated along the same length to build up the Coulomb friction strain range in the "Radial contact model" as the 2D assumption by only including the radial contacts. Therefore, the same Coulomb friction strain range was obtained as the 2D assumption for the large tube. Similar friction effects were also found for the small tube.

However, the Coulomb friction strain ranges of large and small tubes in "Radial and constrained hoop model" was reduced and increased, respectively, by also including the hoop contacts. They were only 7.5% over and 0.4% under estimated as compared to the tests, see Table 5. Figure 19 shows the friction distribution of radial and hoop contact interfaces at zero rocking angle position A as shown in Figure 15. The measured large tube contacted with two small tubes, termed as "Group No.1" and "Group No.3", respectively, see Figure 15. A $\pi/2$ phase angle was observed between the friction distributions of radial and hoop contact interfaces, acting to reduce the friction amplitude as seen in Figure 18. Therefore, the friction force amplitude was reduced to an average of 4116 [N/m] with the same direction along half pitch length in "pitch A", resulting in a 44% decrease of the Coulomb friction strain range for the large tube. Similar friction effects were found for the small tube and Coulomb friction strain range at zero rocking angle position B. It was concluded that it is important to include hoop contacts in addition to the radial contacts for considering the phase effect.

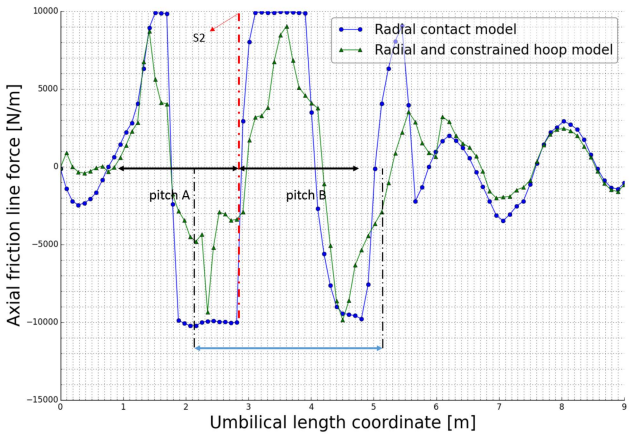

(a) At zero rocking angle position A

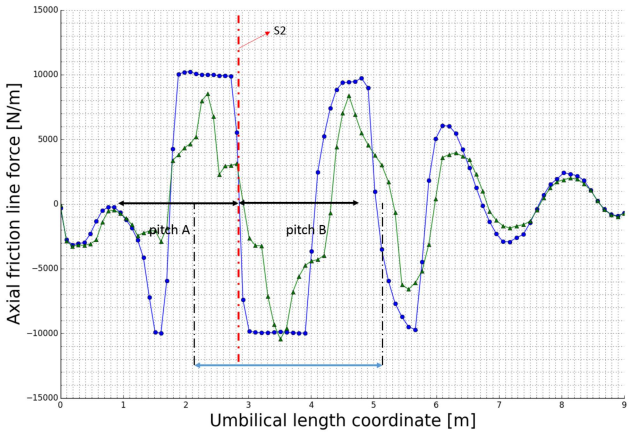

(b) At zero rocking angle position B

Figure 18: Friction force distributions of the large tube at zero rocking angle positions in the "Radial contact model" and "Radial constrained hoop contact model".

Table 5: The Coulomb friction strain range comparison between 2D assumption and 3D FE models based on diffrent contact models

	Coulomb friction strain of large tube [microstrain]	Coulomb friction strain of small tube [microstrain]
Test measurements	200	158
Radial contact model in BFLEX	386	115
Radial and constrained hoop contact model in BFLEX	215	151

Figure 20 shows the friction distributions of large tube in "Radial contact model" and "Radial and constrained hoop contact model" at maximum compressive and tensile axial strain positions C and D which are denoted in Figure 13. In "Radial contact model", the friction force with same direction was developed along 1.2m of large tube in "pitch A" contributing to the maximum compressive strain as seen in Figure 20a. It means that more than a quarter of pitch length of friction force was activated, resulting in building up larger maximum compressive axial strain than that obtained by the 2D assumption. Similar friction effect was also found for the maximum tensile axial strain. However, the extreme axial strain range was underestimated.

For the "Radial and constrained hoop contact model", the maximum compressive axial strain was significantly in-

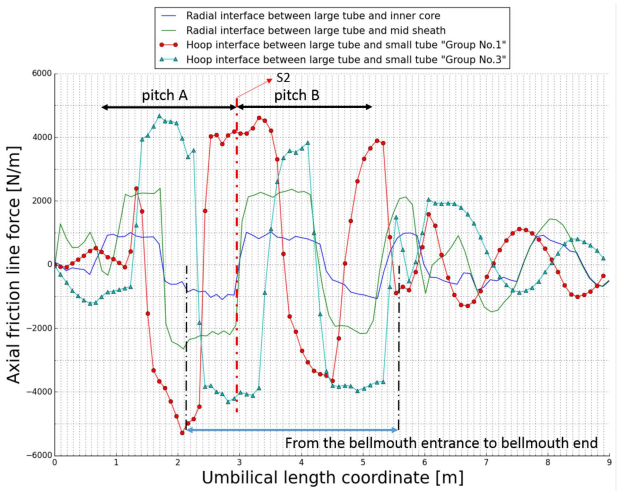

Figure 19: Friction force distribution of radial and hoop contact interfaces in "Radial and constrained contact model".

creased. In Figure 20a, the friction force of elements located from the neutral axis position A1 to S2 was larger than that of the "Radial contact model", resulting in increasing the slip capacity. Then more energy is governed by the elastic energy which is reflected by the significantly increased maximum compressive axial strain with less friction energy dissipation. The maximum tensile axial was reduced because shorter large tube had the same friction direction in "pitch A", as shown in Figure 20b. However, only 0.7% deviation was found with respect to the extreme axial strain range for the large tube. It was concluded that it is important to individually model each helix and include all contact interfaces in the 3D FE model as well as the local constraint effect in order to obtain the extreme value. For the small tube, the extreme axial strain range was underestimated by a 26% deviation.

A sensitivity analysis was carried out by using a friction factor of 0.25 for the "Radial and constrained hoop contact model". The results showed that the extreme axial strain ranges of large and small tubes were over and under estimated by 17% and 11.2%. This implies that the slip capacity is increased with increasing friction coefficient, resulting in more energy being governed by the elastic deformation. The Coulomb friction strain ranges of large and small tubes were 25% and 17% overestimated, respectively, due to the increased friction force.

The resultant curvature range of large tube correlated well with the tests. The measured curvature of small tube in tensile side is 22% larger than that of the bellmouth surface whereas it is 33% smaller in the compressive side, resulting in a total deviation of 12.5%. This might be due to local deformation effects that cannot be captured by the present contact model. However, the resultant curvature at both sides correlated well with the bellmouth surface curvature for both large and small tubes.

6. Conclusions and future work

- Full scale tests were carried out by mounting the fibre-optic braggs inside steel tubes of a 9m long umbilical specimen. The specimen was exposed to constant tension and dynamic curvature by means of two different bellmouth geometries of which one was focused on in the present work. The steel tubes' axial strain and local curvatures were measured. The tests results provided validation data for the local stress analysis where nonlinear effects were observed at extreme rocking angles.
- There existed some uncertain setup parameters including the gap between the bellmouth entrance and the outer sheath as well as the penalty stiffness needed in the contact element to represent the bellmouth geometry. It was found that the axial strain was not sensitive to the gap when the value was smaller than 8mm and a surface contact stiffness 100 $[MN/m^2]$ was found sufficient to describe the bellmouth surface.
- Realizing that the present umbilical cross section is too complex to model by a full 3D model, the strategy adopted in the present work was based on sandwich beam theory with dedicated curved beam elements and

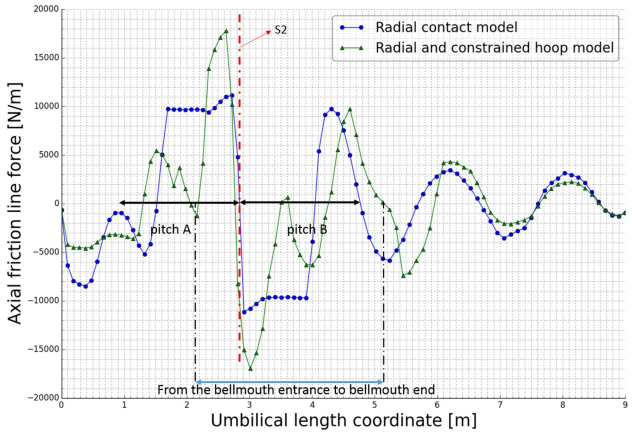

(a) At maximum compressive axial strain C

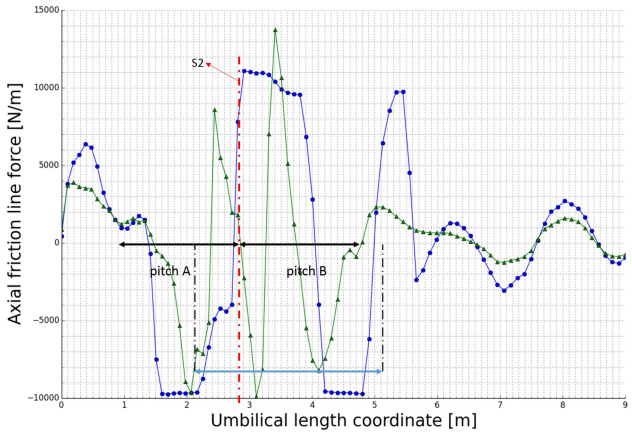

(b) At maximum tensile axial strain D

Figure 20: Friction force distributions of the large tube at maximum compressive and tensile axial strain positions in the "Radial contact model" and "Radial constrained hoop contact model".

associated penalty based contact elements. As hoop contacts existed between steel tubes and separation fillers, a tailor-made contact element was formulated to facilitate the hoop contacts. In addition, individual helix modeling was needed to capture 3D effects observed in the tests. However, it was observed that the fillers and sheath were severely deformed, making it impossible to represent the real contact stiffness based on the idealized cross section. Therefore, a simplified approach was proposed to determine the contact stiffness. It was determined by the interface thickness and Young's modulus as well as the helix diameter. Good correlation was obtained with respect to the axial stiffness, which verified the contact stiffness method to ensure the correct load sharing of internal components.

- As small curvature normally governs the fatigue life, it is important to correctly calculate the Coulomb friction strain range observed in the full scale tests. Two alternatives were used to calculate it by 2D assumption or 3D cyclic bending analysis. The Coulomb friction strain ranges of large and small tubes obtained based on 2D assumption were 87% over and 55% under estimated, respectively, when only including radial contacts. The ranges of large and small tubes were 112% and 162% overestimated by also including hoop contacts. This confirmed the importance of including all contact interfaces in the 2D assumption.

- 3D cyclic bending analyses were carried out by using the "Radial contact model" and "Radial and constrained hoop contact model" where the bellmouth was moved according to the full scale testing procedures under tension 200KN. The Coulomb friction strain range obtained in the "Radial contact model" was similar to the value in the 2D assumption by only including the radial contacts. However, the Coulomb friction strain ranges

of large and small tubes were reduced and increased and had good correlation with the tests by applying the hoop contacts. This was found to be due to a $\pi/2$ phase difference between the friction forces mobilized along the radial and hoop interfaces, acting to reduce the friction force to build up the axial strain. This will act to reduce the conservatism during fatigue calculations.

- The extreme axial strain range of large tube by only including radial contacts was underestimated, however, it correlated well with the tests by also including the constraint effect and hoop contacts. The constraint resulted in redistribution of radial and hoop contact forces and larger friction force distributed along the tube, which means that the full slip capacity was increased. Then more energy was governed by the elastic energy resulting in significantly increasing the deformation of large tube with less friction energy dissipation. These effects can only be described by 3D modeling of each helix which is the only possibility to obtain the correct extreme axial strain range.
- The resultant curvature range of large tube correlated well with the tests. For the small tube, it was deviating 12.5% as compared to the tests. This might be due to local deformation that cannot be captured in the present model.
- The contact stiffness calculated based on the simplified method was only validated for one umbilical specimen. Therefore, it will be beneficial to verify this method by more umbilical full scale testing with respect to axial stiffness.
- The same applies with respect to the dynamic stresses where more data is needed to verify the models specially for bending stiffener cases which govern the majority of flexible riser designs.
- The present contact elements do not include friction coupling between torsion and lateral motions. This should be improved in future work.

Acknowledgments

The authors would like to express our appreciations to Kristian Minde, Emil Bratlie, Nina Langhelle, Janne Kristin Økland Gjøsteen and Dag Fergestad at SINTEF Ocean for their help to understand the testing procedures in the Join Industry Project on Stress and Fatigue Analysis of Umbilicals, Phase II. Dr.Philippe Mainçon is much acknowledged for his help with respect to the test measurements treatment. We also thank the Umbilical JIP sponsors for permitting publishing this article.

References

[1] Svein Sævik. Bflex2010 theory manual. *SINTEF OCEAN*, 2010.

[2] Qianjin Yue, Qingzhen Lu, Jun Yan, Jiexin Zheng, and Andrew Palmer. Tension behavior prediction of flexible pipelines in shallow water. *Ocean Engineering*, 58:201–207, 2013.

[3] Rene Santos Almeida, Wesley Novaes Mascarenhas, Jose Fabio Abreu de Andrade, Antonio Fernando Abreu de Andrade, et al. Application of numerical analysis tools on the performance improvement of umbilicals and their elements. In *OTC Brasil*. Offshore Technology Conference, 2013.

[4] Qing-zhen Lu, Qian-jin Yue, Zhi-xun Yang, Gang Wang, Jun Yan, and Yan Qu. Cross-sectional layout analysis of steel tube umbilical. In *ASME 2012 31st International Conference on Ocean, Offshore and Arctic Engineering*, pages 493–497. American Society of Mechanical Engineers, 2012.

[5] Qingzhen Lu, Zhixun Yang, Jun Yan, and Qianjin Yue. Design of cross-sectional layout of steel tube umbilical. *Journal of Offshore Mechanics and Arctic Engineering*, 136(4):041401, 2014.

[6] Zhixun Yang, Qingzhen Lu, Jun Yan, Jinlong Chen, and Qianjin Yue. Multidisciplinary optimization design for the section layout of umbilicals based on intelligent algorithm. *Journal of Offshore Mechanics and Arctic Engineering*, 140(3):031702, 2018.

[7] AB Custódio and MA Vaz. A nonlinear formulation for the axisymmetric response of umbilical cables and flexible pipes. *Applied Ocean Research*, 24(1):21–29, 2002.

[8] Ian Probyn, Alan Dobson, Michael Martinez, et al. Advances in 3-d fea techniques for metallic tube umbilicals. In *The Seventeenth International Offshore and Polar Engineering Conference*. International Society of Offshore and Polar Engineers, 2007.

[9] Vincent Le Corre and Ian Probyn. Validation of a 3-dimensional finite element analysis model of deep water steel tube umbilical in combined tension and cyclic bending. In *ASME 2009 28th International Conference on Ocean, Offshore and Arctic Engineering*, pages 77–86. American Society of Mechanical Engineers, 2009.

[10] RH Knapp, Terry S Shimabukuro, et al. Structural analysis of composite umbilical cables. In *The Seventeenth International Offshore and Polar Engineering Conference*. International Society of Offshore and Polar Engineers, 2007.

[11] Alan Dobson and Dave Fogg. Fatigue testing and analysis of a deep water steel tube umbilical. In *ASME 2008 27th International Conference on Offshore Mechanics and Arctic Engineering*, pages 133–140. American Society of Mechanical Engineers, 2008.

[12] Ewan Brown et al. Steel tube umbilical design life verification by full-scale fatigue test. In *Offshore Technology Conference*. Offshore Technology Conference, 2011.

[13] Knut I Ekeberg, Mayuresh M Dhaigude, et al. Validation of the loxodromic bending assumption using high-quality stress measurements. In *The 26th International Ocean and Polar Engineering Conference*. International Society of Offshore and Polar Engineers, 2016.

[14] Mayuresh M Dhaigude, Knut I Ekeberg, et al. Validation of the loxodromic bending assumption using high-quality stress measurements–high tension case. In *The 26th International Ocean and Polar Engineering Conference*. International Society of Offshore and Polar Engineers, 2016.

[15] Howard Wang, C Blake Hebert, Gianluca Barbato, Lauro Silveira, Marco Vinicius dos Santos Paiva, Tiago B Coser, Facundo S López, Telmo R Strohaecker, Fabiano Bertoni, et al. Submarine power cable design validation through model testing. In *The 26th International Ocean and Polar Engineering Conference*. International Society of Offshore and Polar Engineers, 2016.

[16] Marco Vinicius dos Santos Paiva, Lauro Silveira, Howard Wang, C Blake Hebert, Tiago B Coser, Facundo S López, Telmo R Strohaecker, Fabiano Bertoni, et al. Validation of power cable local stress analysis. In *The 26th International Ocean and Polar Engineering Conference*. International Society of Offshore and Polar Engineers, 2016.

[17] Fergestad Dag, Janne Gjøsteen, and Philippe Mainçon. *Umbilical JIP-Phase II, full scale testing of specimen No.1*. SINTEF OCEAN, 2011.

[18] JK Gjøsteen and S Sævik. Expermiental validation of a 3-dimensional umbilical cross-section model. *International Conference on Floating Structures for Deepwater Operations*, pages 21–23, 2009.

[19] Svein Sævik. Bflex2010 user manual. *SINTEF OCEAN*, 2010.

[20] TY Chang, AF Saleeb, and SC Shyu. Finite element solutions of two-dimensional contact problems based on a consistent mixed formulation. *Computers & structures*, 27(4):455–466, 1987.

[21] SC Shyu, TY Chang, and AF Saleeb. Friction-contact analysis using a mixed finite element method. *Computers & structures*, 32(1):223–242, 1989.

[22] Svein Sævik. Uflex theory manual. *SINTEF OCEAN*, 2015.

[23] Tianjiao Dai, Svein Sævik, and Naiquan Ye. Friction models for evaluating dynamic stresses in non-bonded flexible risers. *Marine Structures*, 55:137–161, 2017.

[24] Tianjiao Dai, Svein Sævik, and Naiquan Ye. An anisotropic friction model in non-bonded flexible risers. *Marine Structures*, 59:423–443, 2018.

[25] Geir Skeie, Nils Sødahl, and Oddrun Steinkjer. Efficient fatigue analysis of helix elements in umbilicals and flexible risers: Theory and applications. *Journal of Applied Mathematics*, 2012, 2012.

Conflict of Interest

Declaration of interests

☒ The authors declare that they have no known competing financial interests or personal relationships that could have appeared to influence the work reported in this paper.

☐The authors declare the following financial interests/personal relationships which may be considered as potential competing interests: